# Very high cycle fatigue durability of an additively manufactured single-crystal Ni-based superalloy

Luciana Maria Bortoluci Ormastroni[1, *], Inmaculada Lopez-Galilea[2], Julian Pistor[3], Benjamin Ruttert[2], Carolin Körner[3], Werner Theisen[2], Patrick Villechaise[1], Fernando Pedraza[4], and Jonathan Cormier[1, *]

[1] Institut Pprime, UPR CNRS 3346, Physics and Mechanics of Materials Department, ISAE-ENSMA, 1 avenue Clément Ader, BP 40109, 86961 Futuroscope-Chasseneuil Cedex, France.
[2]Ruhr-Universitat Bochum, Institut fur Werkstoffe, lehrstuhl Werkstofftechnik, Universitasstr. 150, D-44801 Bochum, Germany.
[3]Friedrich-Alexander-Universität Erlangen-Nürnberg, Department Werkstoffwissenschaften, Lehrstuhl für Werkstoffwissenschaften, Martensstr. 5, D-91058 Erlangen, Germany.
[4]Université de La Rochelle, Laboratoire des Sciences de l'Ingénieur pour l'Environnement (LaSIE UMR-7356 CNRS), Avenue Michel Crépeau, 17042 La Rochelle, cedex 01 – France

*Corresponding authors: luciana-maria.bortoluci-ormastroni@ensma.fr, jonathan.cormier@ensma.fr

**Highlights**

- Additively manufactured and Bridgman solidified CMSX-4 superalloy have comparable VHCF life under high temperature.
- The superalloy chemistry controls the fatigue life of defect-free specimens.
- Defect-free specimens fails by surface crack initiation.
- The fatigue limit is controlled by the superalloy oxidation resistance at temperature of 1,000 °C.

**Abstract**

A single crystalline (SX) nickel-based superalloy additively manufactured (AM) by electron beam-based powder bed fusion (PBF-E) was investigated under very high cycle fatigue (VHCF) at 1,000 °C in fully reversed conditions ($R_\varepsilon$ = -1). Specimens processed using a classical Bridgman solidification route and the impact of a hot isostatic pressing (HIP) treatment were also considered. It is shown that the fatigue lifetime of the AM specimens is higher or in the same range of the Bridgman processed ones with the same chemical composition. All defect-free AM samples fail by surface initiation with very long VHCF lives. In the absence of metallurgical defects such as grain boundaries or pores, the superalloy chemical stability against oxidation governs VHCF failure.

*Keywords: Nickel-based superalloys, additive manufacturing, electron beam-based powder bed fusion, very high cycle fatigue.*

Paper Accepted in Additive Manufacturing 9 March 2022. https://doi.org/10.1016/j.addma.2022.102759

## 1 Introduction

Nickel-based superalloys in single-crystalline (SX) form are widely used in the hot-sections of aero-engines for the manufacturing of blades and vanes thanks to their excellent mechanical properties at temperatures up to ≈ 90 % of the material's melting temperature [1,2]. During service operations at (very) high temperatures, these components undergo a variety of damages including creep, corrosion, and oxidation [2–4]. The entire replacement of damaged components results in material and time costs. The use of additive manufacturing (AM) techniques allows for the design of turbine blades with complex geometrical designs (e.g., intricate cooling channels) combined with the possibility of refurbishment. Electron beam based powder bed fusion (PBF-E) is one of the methods that can be adopted by the industry in the near future [5]. One of the most promising interests in employing PBF-E to produce Ni-based SX superalloys is to control different processing parameters to obtain a superalloy with specific microstructural characteristics [6].

CMSX-4 is one of the "legacy" Ni-based SX superalloys used in the hottest-sections of civil and military aero-engines as blade material [1,7,8]. It is a $\gamma/\gamma'$ superalloy which presents a quite high degree of chemical segregation after casting compared to first generation Ni-based SX superalloys. A specific full heat treatment (HT) with subsequent aging(s) (AG) is required to obtain a desired $\gamma'$ size and volume fraction so as to optimize mechanical properties, especially monotonic ones [6,9–11]. A collaboration between Cannon-Muskegon, the producer of CMSX-4 alloy, and the research center SFB/TR 103 [12] allows SFB/TR 103 to reproduce this superalloy chemistry for the subsequent preparation of SX PBF-E bars.

Considering that fatigue is responsible for most of the crack initiation events/failure cases of internally cooled blades of aero-engines [13], it is of utmost importance to investigate fatigue properties of a PBF-E processed SX superalloy, especially in the very high cycle fatigue (VHCF) regime in view of using such a processing route for the manufacturing of Ni-based SX airfoils in future aero-engines. Fatigue tests under high and very high temperatures with a lifetime higher than $10^8$ cycles are very time consuming using a conventional fatigue machine (≈ 100 Hz). Ultrasonic machines (in the kHz regime) became a solution in order to study the damage mechanisms at very high vibratory frequencies [14]. It is also recalled that HCF/VHCF durability is a certifying criteria of airfoils according to airworthiness authorities (e.g. EASA and FAA) [15–17], as the loading by vibratory stresses turns out to be a matter of safety requirement of aero-engines.

From the authors' very best knowledge, there is only one published study focused on the fatigue properties of a PBF-E SX superalloy in the low cycle fatigue (LCF) regime [9]. In fact, Meid et al. investigated the PBF-E SX performance of CMSX-4 alloy in stress-controlled LCF at 950 °C/0.25 Hz and $R_\sigma = 0.6$ [9]. It was shown in this pioneering study that the PBF-E SX alloy can perform similar to the conventionally processed SX alloy, provided that an adequate heat treatment sequence is performed after the AM process. This result is not surprising considering the fact that in such LCF conditions (high temperature, high mean stress, low frequency), a pronounced cyclic ratcheting is observed, indicating that creep damage is also contributing to the overall LCF durability [9].

In contrast, the present paper focuses on the durability of the same PBF-E SX alloy in the VHCF domain at high temperature/ $R_\varepsilon = -1$. In such conditions, the VHCF life of conventionally processed Ni-based SX superalloys is known to be highly dependent on the solidification parameters [14–20]. In fact, VHCF crack initiation occurs at the largest casting pores in nearly 95 % of the cases at $R_\varepsilon = -1/1000$ °C [15,17,19,20] and only occasionally at the

surface due to oxidation [15,19,21,22] or due to a prior plastic deformation, inducing surface recrystallization [23]. VHCF life in fully reversed conditions at high temperature is hence really sensitive to the presence of defects such as pores and/or grain boundaries. In the absence of large solidification pores in the PBF-E material due to the AM process itself [24,25], a better fatigue performance is expected and/or different crack initiation mechanisms, but this needs to be investigated and therefore, it constitutes the main objective of this manuscript.

To achieve this aim, the PBF-E CMSX-4 SX samples have been tested with and without hot isostatic pressing (HIP) treatment [15,25,26] in the present investigation. The results were compared with the database available from the literature [15] using a Bridgman-processed CMSX-4 alloy after full HT, established using the same VHCF set-up.

## 2 Materials and methods

### *2.1. Chemical composition and heat treatments*

The nominal chemical compositions of CMSX-4/Bridgman, ERBO/1 and CMSX-4 atomized powder used to build PBF-E specimens is listed in **Table 1**.

**Table 1**

CMSX-4/Bridgman, ERBO/1, and CMSX-4 atomized powder nominal chemical compositions (in wt. pct.).

| **Alloy** | **Ni** | **Cr** | **Mo** | **Co** | **W** | **Re** | **Al** | **Ti** | **Ta** | **Hf** |
|---|---|---|---|---|---|---|---|---|---|---|
| **CMSX-4/Bridgman** [15] | Bal. | 6.5 | 0.6 | 9.0 | 6.0 | 3.0 | 5.6 | 1.0 | 6.35 | 0.1 |
| **ERBO/1** [27] | Bal. | 6.2-6.6 | 0.5-0.7 | 9.3-10.0 | 6.2-6.6 | 2.8-3.1 | 5.4-5.75 | 0.9-1.1 | 6.3-6.75 | 0.07-0.12 |
| **CMSX-4 Atomized powder** [31] | Bal. | 6.6 | 0.6 | 9.9 | 6.4 | 2.9 | 6.2 | 1.1 | 6.6 | 0.08 |

The CMSX-4/Bridgman fatigue results are extracted from the literature [15]. For this reason, the HT was described in the previous article [15]. The ERBO/1 plate used to machine the fatigue specimens was provided by Doncasters Bochum company in partnership with the Ruhr-Universitat Bochum. This plate had a 20 mm thickness. The HT (ERBO/1C according to [27]) was presented in the literature [27].

Square bars with 12 mm edges were built (**Fig.1 a**) by the PBF-E method. The PBF-E CMSX-4 SX samples were divided in two different groups depending on whether they have or not a HIP treatment. First, the AM/HT/REC (AM: Additive manufacturing, HT: Heat treated, REC: Recycled atomized powder) specimens were built with recycled powder, HT by standard method in air at 1,315 °C/35 min and finally aged at 1,140 °C/2 h/AQ (air quench) and at 870 °C/20 h/AQ. The AM/HIP (HIP: HIP treatment) specimens were homogenized in the QIH-9 HIP (hot isostatic pressing) at 1,315 °C/35 min under 100 MPa Argon pressure. The material was directly quenched after holding by applying the fast-cooling capability of the HIP set-up to achieve ultrafine γ' precipitates. Then, the

material was subjected to the same AG treatment as defined for the non-HIPed material. The AM/HIP samples were received in two different batches. The first batch containing eight bars had been built using recycled powder (AM/HIP/REC). The second batch contained four bars fabricated with fresh powder (AM/HIP/FRS) (FRS: Fresh atomized powder). The nomenclature is detailed in **Table 2**.

**Table 2**

Sample's nomenclature. HT is the denomination for full heat treatment. PBF-E is the denomination for electron beam based powder bed fusion. SHT is the denomination for solution heat treatment. AG is the denomination for aging treatment. AQ is the denomination for air quench. HIP is the denomination for hot isostatic pressing.

| Nomenclature | Superalloy/Solidification process/Heat treatment |
|---|---|
| **CMSX-4/Bridgman** | CMSX-4 solidified by classical Bridgman method → HT described in the literature [15] |
| **ERBO/1** | ERBO/1 solidified by classical Bridgman method → HT described in the literature as ERBO/1C [27] |
| **AM/HT/REC** | Additive manufacturing (PBF-E) samples built w/ recycled CMSX-4 atomized powder → SHT in air at 1,315 °C/35 min and AG steps at 1,140 °C/2 h/AQ and 870 °C/20 h/AQ |
| **AM/HIP/REC** | Additive manufacturing (PBF-E) samples built w/ recycled CMSX-4 atomized powder → HIP homogenization at 1,315 °C/35 min under 100 MPa Argon pressure |
| **AM/HIP/FRS** | Additive manufacturing (PBF-E) samples built w/ fresh CMSX-4 atomized powder → HIP homogenization at 1,315 °C/35 min under 100 MPa Argon pressure |

*2.2. Stereological analyzes*

A γ/γ' stereological analysis was performed using a JEOL JSM-7000F scanning electron microscope, by applying the secondary electron imaging (SEI) mode operating at 25 kV. The microstructures are shown in **Fig. 1 b-g**. The observations have been made in both primary dendrite arms (D) and interdendritic spacing (ID) for Bridgman processed CMSX-4/Bridgman and ERBO/1 alloys. As the PBF-E processed alloy has very small primary dendrite arms spacings [6,31], almost no remaining difference in precipitate size and morphology can be observed in a fully heat treated/HIPed state across this very fine dendritic structure (**Fig. 1 f-g**). The software ImageJ was employed to analyze the γ' size. All measurements were done in the dendrite core for Bridgman solidified alloys. The γ' average edge length of CMSX-4/Bridgman alloy is 590 ± 120 nm, and it is 560 ± 80 nm for the ERBO/1 one. The AM/HT/REC presents 420 ± 80 nm, and AM/HIP/REC 470 ± 100 nm sizes. The average edge length of γ' precipitates in the PBF-E SX is hence smaller compared to the one in CMSX-4/Bridgman and ERBO/1 materials. This difference in γ' size between all the investigated specimens has been neglected in the following of this article since it is known from the prior literature that the VHCF properties of Ni-based SX superalloys are not dependent on the precipitation size and morphology at $R_\varepsilon$ = -1/1000 °C [17]. Moreover, a possible small variation in γ' volume fraction around 70 % does not seem neither to have any impact on the VHCF properties in these conditions [15].

The CMSX-4 PBF-E SX stereological characterization detailed in [25,29,30] has shown that the SX part developed pores having a ≈ 1.7 µm average diameter size [24,25], which contrasts with the Bridgman method that results in solidification pores of up to 200 µm after the complete solution heat treatment (SHT) for this alloy [28].

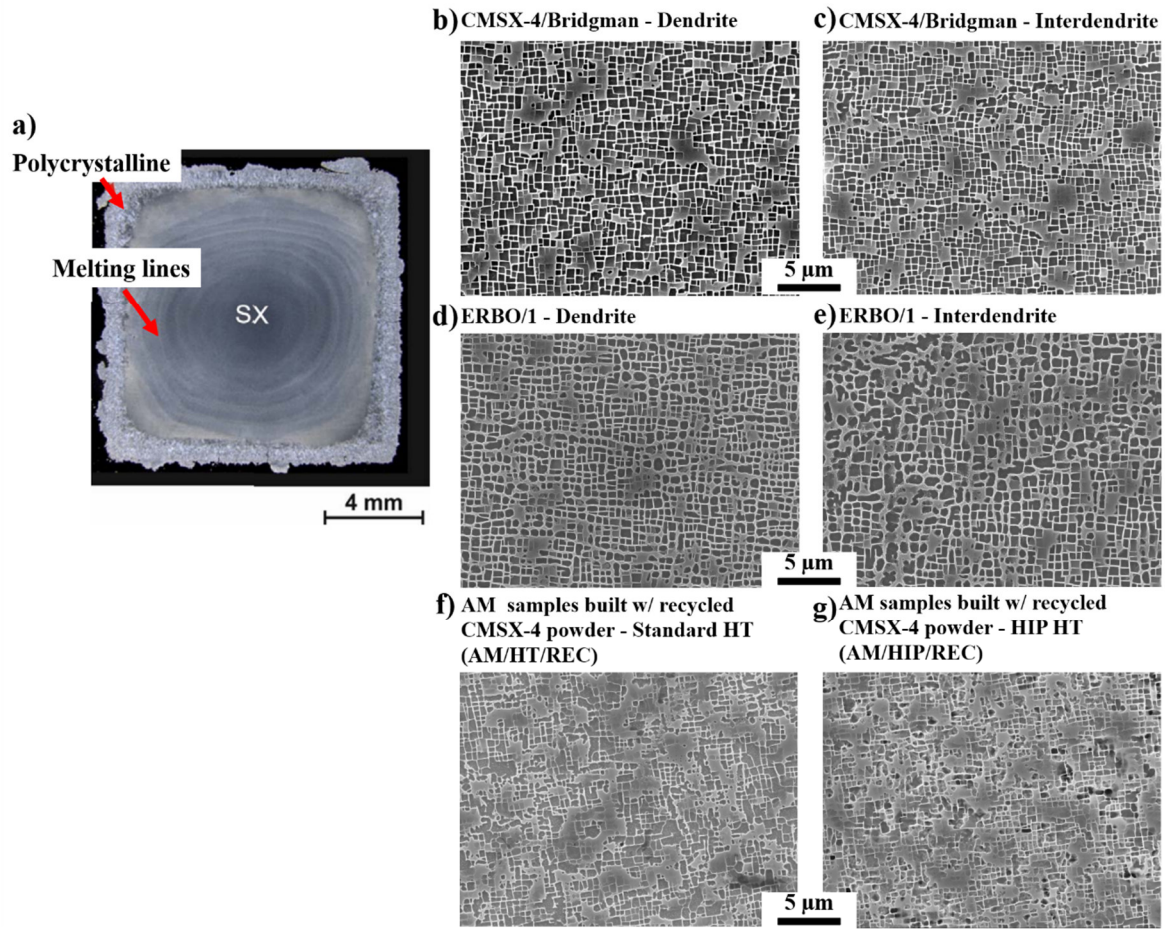


**Fig. 1.** (a) PBF-E SX 12 mm square bars microstructure details (aqua regia etched). (b) γ/γ' microstructure of CMSX-4/Bridgman observed in primary dendrite arms and (c) in interdendritic spacing. (d) ERBO/1 alloy solidified by a Bridgman method in primary dendrite arms and (e) in interdendritic spacing. (f) CMSX-4 alloy processed by PBF-E after standard heat treatment and (g) after HIP treatment.

*2.3. Specimens' machining and very high cycle fatigue tests details*

VHCF tests were performed using hourglass-shaped samples (see **Fig. 2**) [32]. The samples were extracted by electric discharge machining and subsequent turning to reach the final shape. Two samples for AM/HT/REC, twelve samples for AM/HIP of the two batches (8 specimens AM/HIP/REC and 4 specimens AM/HIP/FRS) and eight samples for ERBO/1 were machined at Pprime Institute. A thickness of 0.2 mm from the original diameter was first removed by SiC grinding to remove residual stresses inherited from the machining steps. This polishing step was essential to avoid surface recrystallization during the fatigue tests at high temperature. Thereafter, the

surfaces were gently ground and polished to a final mirror polish (1 µm diamond suspension) with the final steps parallel to the loading axes.

Strain-controlled VHCF tests were performed at 1,000 °C (± 2 °C), f = 20 ± 0.5 kHz, $R_\varepsilon$ = -1 with an ultrasonic fatigue machine used in previous studies [16–19,21,23,32]. The fatigue tests were performed with a sinusoidal waveform. These tests were performed using alternating stresses allowing i) a direct comparison with conventionally processed Ni-based single crystalline specimens previously tested at Institut Pprime [16–19,21,23,32], ii) a good control of specimen's temperature and iii) failure of specimens in a reasonable time. An induction coil was used as a heating source, the power of which was controlled by a closed loop with a dual-wavelength pyrometer measuring the specimen's central temperature. A pre-heating of 45 min at 1,000 °C was applied before starting the tests to stabilize the surface oxides and resulting surface emissivity. Due to the high density of dislocations stored in the AM processed specimens, especially in the HIPped ones, only low alternating stresses were used to limit the impact of specimens' self-heating on their temperature control. Hence, AM specimens were all tested with an alternating stress $\sigma_a$ below 180 MPa. With this high temperature VHCF set-up used in these previously described conditions, fluctuations in alternating stress of +/- 3 MPa at maximum have been observed throughout tests.

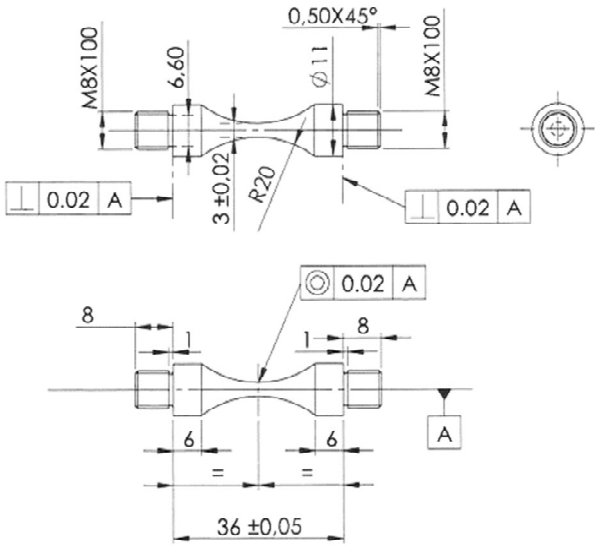


**Fig. 2.** Ultrasonic fatigue sample dimensions (in mm), used for VHCF tests at 1,000 °C.

*2.4. Post-mortem analyses*

Optical and scanning electron microscopy (OM and SEM, respectively) were employed to perform post-mortem observations. Fractographic analyses were carried out using a field emission gun (FEG) microscope JEOL JSM-7000F operating at 25 kV. The longitudinal sections were mirror polished down to 1 µm to observe the microstructure under secondary (SEI) and backscattered electrons (BSE) imaging modes in the same equipment operating at ≈10 mm work distance. The chemical analyses were conducted with an EDAX energy dispersive spectrometer (EDS). The analyses were made on un-etched surfaces to avoid any potential dissolution of oxides, carbides and other metallurgical phases that could fake the interpretation. In addition, electron backscatter

diffraction (EBSD) analyses were performed to characterize the crystallographic orientation around the internal crack initiation. It was performed using a second JEOL JSM-6100 SEM, operating at 25 kV, and the orientation imaging microscopy (OIM) software EDAX, version 6.1. A 0.2 µm scanning step was chosen. The specimens were polished using colloidal silica solution (particle size 0.04 µm).

## 3 Results

### *3.1. VHCF performances and fractographic analyses*

The alternating stress ($\sigma_a$) as a function of the number of cycles to failure (Nf) diagram gathering all VHCF results obtained in the present study is presented in **Fig. 3**. It can also be observed that fatigue lives ranging from $\approx 10^6$ cycles up to $\approx 3.0 \times 10^{10}$ cycles have been obtained at $\sigma_a$ = 145 MPa. The latter is probably the longest fatigue test ever performed on this class of alloy at high temperature. Significant scattering in ERBO/1 can result from different crack initiation mechanisms that will be detailed later in this article.

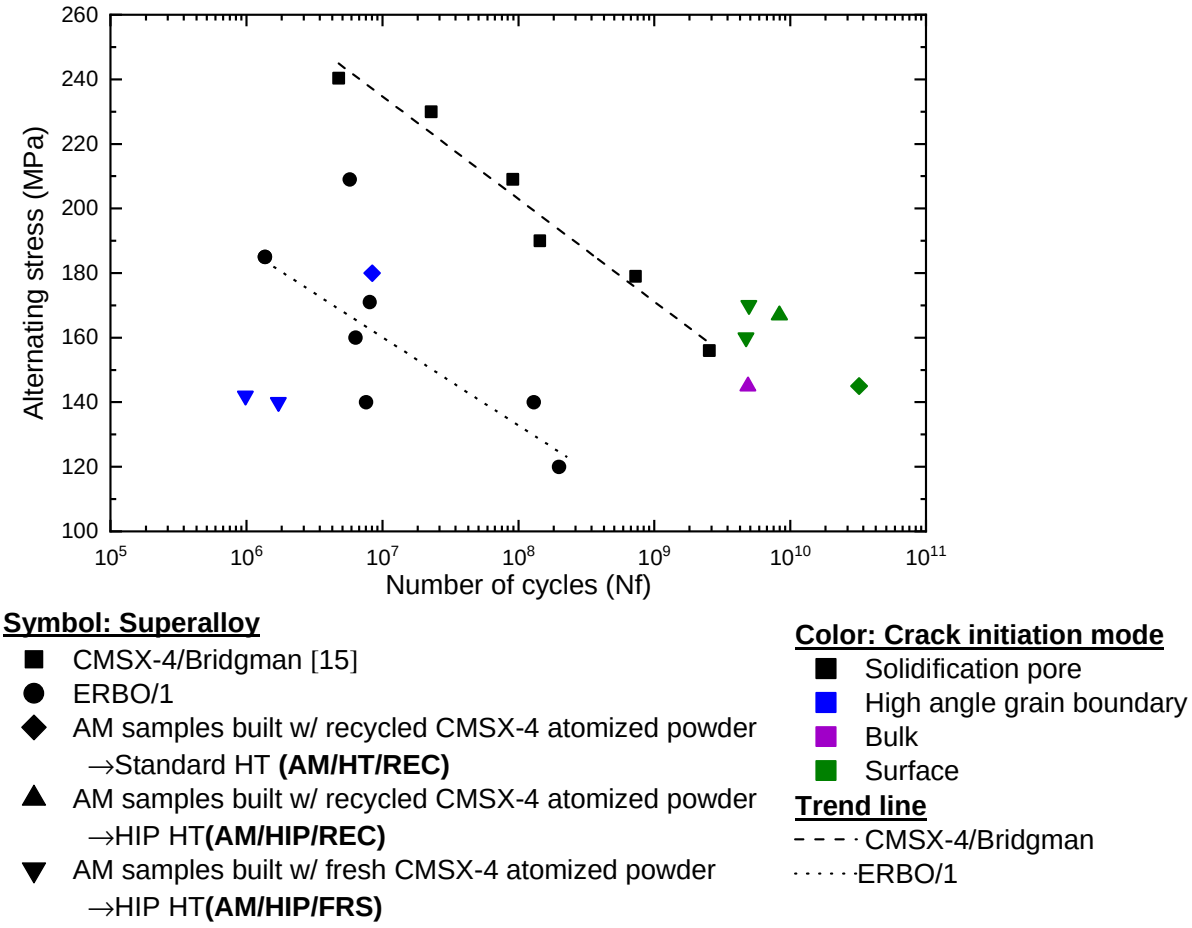


**Fig. 3.** S-N diagram at 1,000 °C, $R_\varepsilon$ = -1 / f = 20 kHz. The alternating stress $\sigma_a$ is plotted as a function of the number of cycles to failure. The CMSX-4/Bridgman data, represented with black squares, were extracted from the literature [15]. (For interpretation of the references to color in this figure legend, the reader is referred to the web version of this article.)

The AM processed specimens present very different VHCF lives, either very long ones in excess of $5.0 \times 10^9$ cycles, or short ones below $10^7$ cycles. In fact, six AM/HIP/REC samples failed from stray grains, which presumably formed during the PBF-E and/or HIPing processes. The presence of such grains within the gauge part of VHCF specimens, especially close to the surface, results in very low VHCF lives. Failure during the initial ramping-up in alternating stress up to reaching the desired value in $\sigma_a$ even occurred in six different samples containing stray grains (**Fig. 4** and **Table 3**). These tests were considered as "unsuccessful" since no stabilized alternating stress was reach.

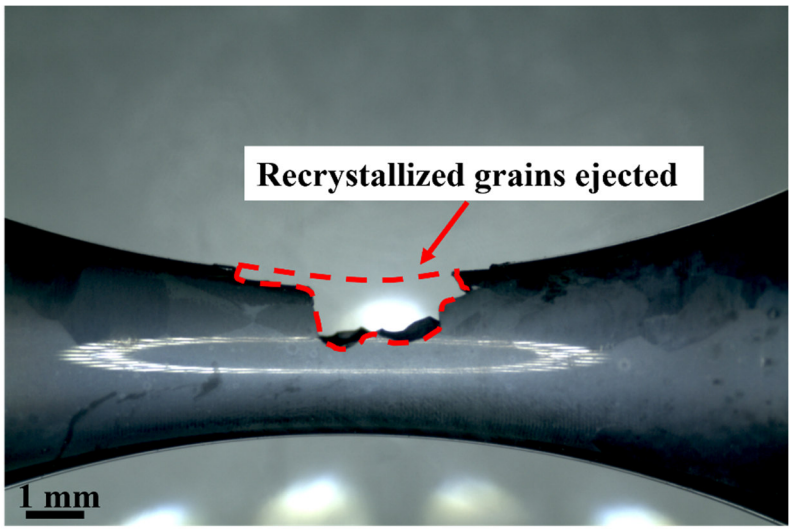


**Fig. 4.** Optical microscope observations of two AM/HIP/REC samples that presented immediate failure. The red dotted region illustrates the location of a recrystallized grains ejected from the specimen gauge part during the application of the alternating stress.

All other successful tests using PBF-E processed specimens (i.e., AM/HT/REC, AM/HIP/REC and AM/HIP/FRS samples) with a few cycles close to the CMSX-4/Bridgman trend line failed from a surface crack initiation or from an internal site (see **Fig. 3**). The presence of grain boundaries within the gauge part of specimens appears to be detrimental to the VHCF life of AM processed specimens and may lead to fatigue lives well below the ones obtained for Bridgman processed alloys (see **Fig. 3** and **Table 3**).

After mechanical testing, fractographic observations were performed. The fracture analysis of CMSX-4/Bridgman specimens was already presented in detail by Cervellon et al. [15]. Crack initiation from internal solidification pores was systematically obtained, these critical pores having a maximum diameter ranging from 50 to 150 µm [15]. In good agreement with this reference database, ERBO/1 specimens systematically presented a crack initiation from solidification pores with a size ranging from 80 to 200 µm (see **Table 3** and **Fig. 5**). Such a crack initiation mode has already been well explained in the literature [15,20,32]. The quite pronounced scatter in VHCF life of ERBO/1 specimens displayed in **Fig. 3** results from the quite large variation in casting pore size serving as the main crack initiation site (**Fig. 5)**, since specimens were machined out from a thick SX plate. In fact, using the same casting parameters, large SX castings are known to introduce larger solidification pores, overall reducing the VHCF life [15]. Hence, the variability in VHCF life of ERBO/1 does not deserve further analysis/discussion.

Focusing on the successful results shown in **Fig. 3** for PBF-E-processed specimens (i.e., no consideration of specimens containing high angle grain boundaries), most of AM/HT/REC, AM/HIP/REC and AM/HIP/FRS samples presented crack initiation at the surface, as shown in **Fig. 6**. According to **Fig. 6**, surface cracks assisted by oxidation as deep as 0.8 mm have been observed after failure. The fracture surfaces of these specimens are also characterized by a subsequent crack propagation zone in mode I (highlighted by yellow dotted lines), which seems to be less oxidized according to the lighter contrast, and then by a final failure area in shear mode. Specimens with a high VHCF life ($Nf > 4 \times 10^9$ cycles) presented several surface cracks (secondary cracks) that were perpendicular and parallel to the main loading axis, as shown in **Fig. 7** for two different specimens tested at $\sigma_a = 145$ MPa. Both specimens present a non-negligible density of surface cracks. However, the main crack initiation site was not necessarily at the specimen's surface (see **Table 3** and **Fig. 8a**). In fact, only one specimen had crack initiation from an internal site (AM/HIP/REC-2, see **Fig. 8b**) with the characteristic rough zone commonly observed around the main crack initiation site of samples tested under VHCF conditions [15,20], see yellow insert in **Fig. 8b**. However, it was not possible to unambiguously conclude on the nature this crack initiation site from fractographic observations and further observations along longitudinal cuts were thus performed.

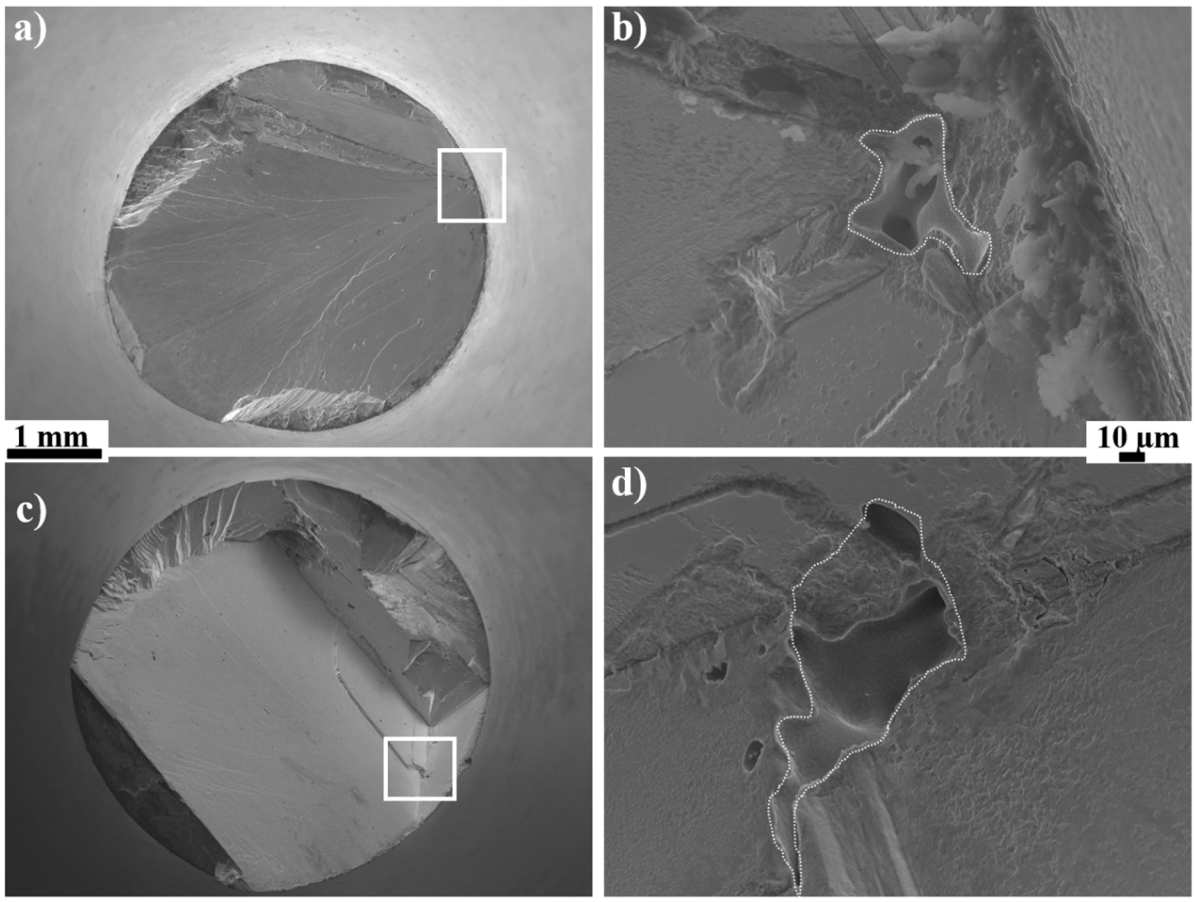


**Fig. 5.** Fractographic observations of ERBO/1 samples with main crack initiation from solidification pores. (a) ERBO/1-6 ($\sigma_a = 209$ MPa, with $Nf = 5.7 \times 10^6$ cycles) and (b) crack zone magnification, detail to the presence of a casting pore close to the surface with diameter of ≈ 40 µm. (c) ERBO/1-1 ($\sigma_a = 160$ MPa, with $Nf = 6.6 \times 10^6$ cycles) and (d) crack zone magnification, detail to the presence of a casting pore with diameter of ≈ 170 µm.

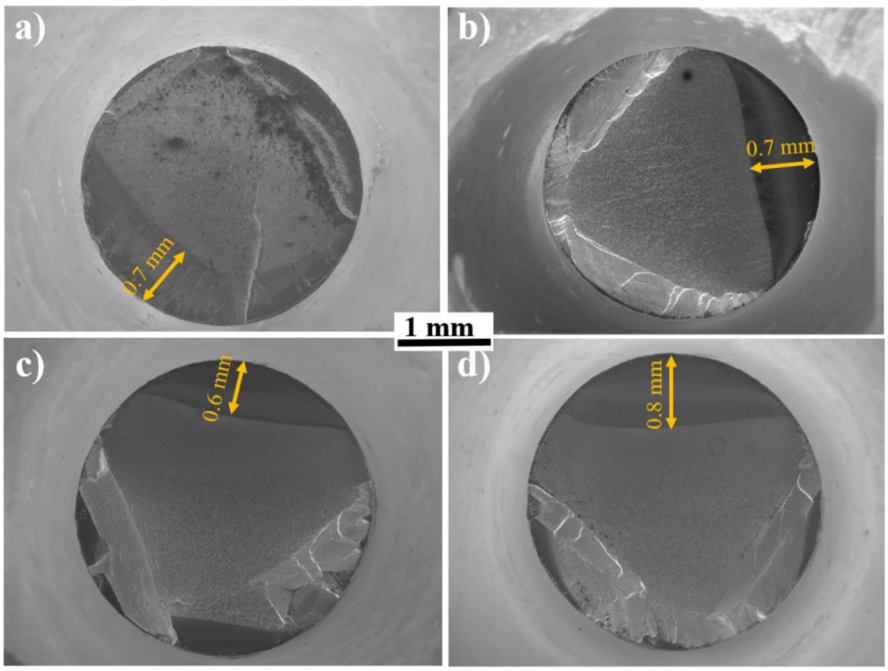


**Fig. 6.** Fractographic observations of PBF-E processed specimens with main crack initiation from the surface: (a) AM/HT/REC-1 ($\sigma_a$ = 145 MPa, Nf = 3.2 × $10^{10}$ cycles), (b) AM/HIP/REC-1 ($\sigma_a$ = 167 MPa, Nf = 8.3 × $10^9$ cycles), (c) AM/HIP/FRS-2 ($\sigma_a$ = 170 MPa, Nf = 4.9 × $10^9$ cycles), (d) AM/HIP/FRS-3 ($\sigma_a$ = 160 MPa, Nf = 4.7 × $10^9$ cycles). The maximum depth of the main fatal crack initiated at the surface is added for each specimen.

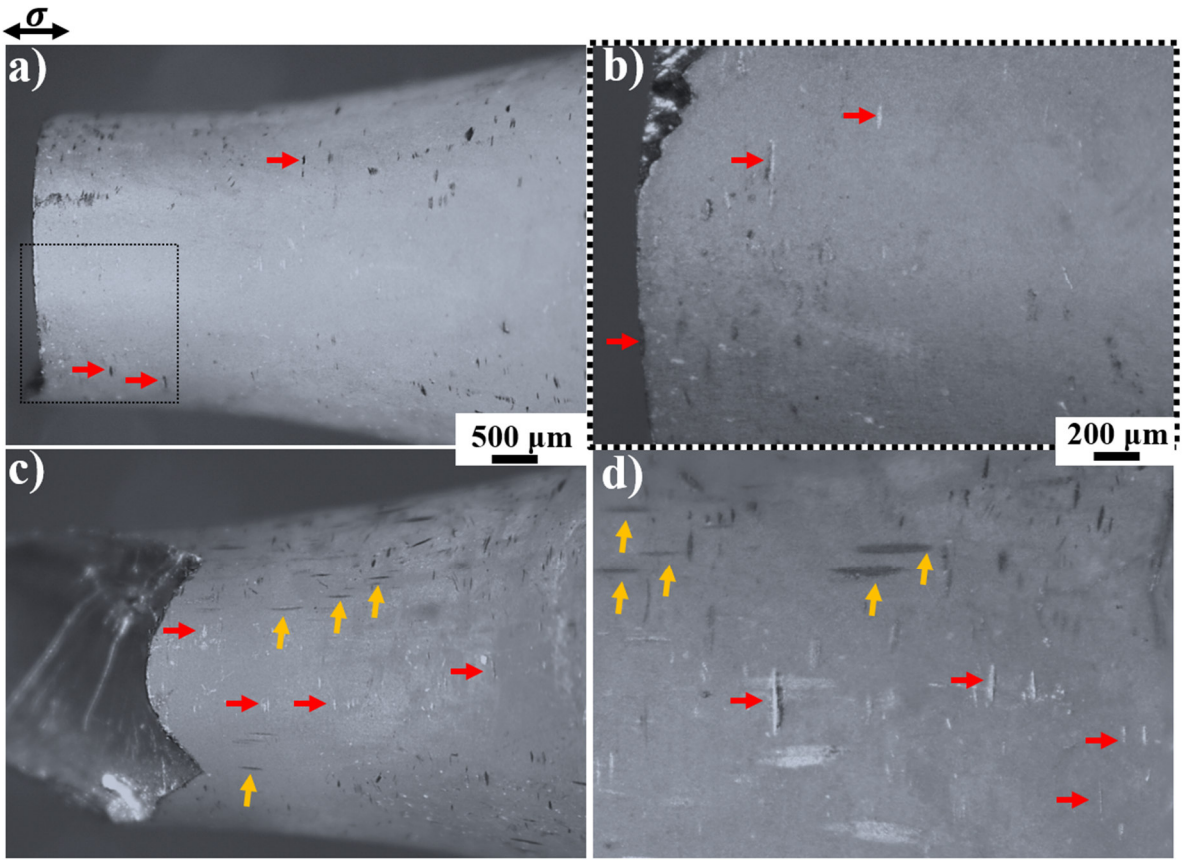


**Fig. 7.** Two examples of PBF-E processed specimens with surface cracks. (a and b) AM/HT/REC-1 and (c and d) AM/HIP/REC-2. Both tests were performed at $\sigma_a$ = 145 MPa, with Nf = $3.2 \times 10^{10}$ cycles for AM/HT/REC-1 and Nf = $4.9 \times 10^{9}$ cycles for AM/HIP/REC-2. Red and yellow arrows indicate, respectively, cracks perpendicular and parallel to the loading axis. (For interpretation of the references to color in this figure legend, the reader is referred to the web version of this article.)

**Table 3**

VHCF results at 1,000°C/$R_\varepsilon$ = -1/f = 20 kHz of Bridgman and PBF-E processed ERBO/1 SX specimens.

| | Specimen | $\sigma_a$ (MPa) | Nf (cycles) | Crack initiation |
|---|---|---|---|---|
| PBF-E | **AM/HT/REC-1** | 145 | $3.2 \times 10^{10}$ | Surface initiation |
| | **AM/HT/REC-2** | 180 | $8.4 \times 10^{6}$ | High angle grain boundary |
| | **AM/HIP/REC-1** | 167 | $8.3 \times 10^{9}$ | Surface initiation |
| | **AM/HIP/REC-2** | 145 | $4.9 \times 10^{9}$ | Bulk initiation |
| | **AM/HIP/REC-3** | | | Immediate failure during alternating stress ramp-up |
| | **AM/HIP/REC-4** | | | Immediate failure during alternating stress ramp-up |
| | **AM/HIP/REC-5** | | | Immediate failure during alternating stress ramp-up |
| | **AM/HIP/REC-6** | | | Immediate failure during alternating stress ramp-up |
| | **AM/HIP/REC-7** | | | Immediate failure during alternating stress ramp-up |
| | **AM/HIP/REC-8** | | | Immediate failure during alternating stress ramp-up |
| | **AM/HIP/FRS-1** | 142 | $9.8 \times 10^{5}$ | High angle grain boundary |
| | **AM/HIP/FRS-2** | 170 | $4.9 \times 10^{9}$ | Surface initiation |
| | **AM/HIP/FRS-3** | 160 | $4.7 \times 10^{9}$ | Surface initiation |
| | **AM/HIP/FRS-4** | 140 | $1.7 \times 10^{6}$ | High angle grain boundary |
| Bridgman | **ERBO-BR-1** | 160 | $6.3 \times 10^{6}$ | Solidification pore |
| | **ERBO-BR-2** | 140 | $7.6 \times 10^{6}$ | Solidification pore |
| | **ERBO-BR-3** | 120 | $1.9 \times 10^{8}$ | Solidification pore |
| | **ERBO-BR-4** | 171 | $8.0 \times 10^{6}$ | Solidification pore |
| | **ERBO-BR-5** | 140 | $1.3 \times 10^{8}$ | Solidification pore |
| | **ERBO-BR-6** | 209 | $5.7 \times 10^{6}$ | Solidification pore |
| | **ERBO-BR-7** | 185 | $1.3 \times 10^{6}$ | Solidification pore |
| | **ERBO-BR-8** | 185 | $2.6 \times 10^{7}$ | Solidification pore |

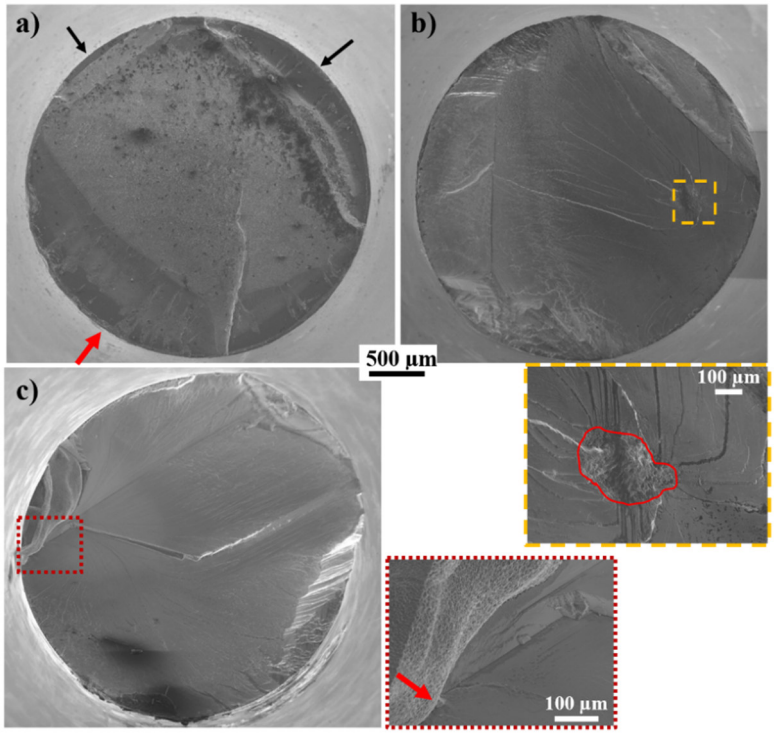


**Fig. 8.** Fractographic observations of three PBF-E processed specimens: (a) AM/HT/REC-1 ($\sigma_a$ = 145 MPa, Nf = 3.2 × $10^{10}$ cycles) with surface crack initiation pointed by the arrows, the main initiation is highlighted by the red arrow; (b) AM/HIP/REC-2 ($\sigma_a$ = 145 MPa, Nf = 4.9 × $10^9$ cycles) with a main internal crack site, presenting the characteristic rough zone pointed by the dotted yellow square (see insert); and (c) AM/HIP/FRS-1 ($\sigma_a$ = 142 MPa, Nf = 9.8 × $10^5$ cycles) with a main initiation from a surface grain boundary pointed by the red dotted square (see insert). (For interpretation of the references to color in this figure legend, the reader is referred to the web version of this article.)

### *3.2. Microstructure investigation along longitudinal sections*

The longitudinal cross-sections were prepared in AM/HT/REC-1 and AM/HIP/REC-2 specimens to better understand crack initiation mechanisms for both PBF-E processed specimens.

#### *3.2.1. Crack initiation from an internal site: AM/HIP/REC-2 specimen*

The crack initiation site observed in **Fig. 8b** has been investigated at a high magnification and along a longitudinal section intercepting the initiation site as shown in **Fig. 9**. Different imaging modes have been used to try to determine its exact nature. From this figure, it was possible to identify needle-shaped precipitates (red arrows in **Fig. 9 c**). The rough zone presented discontinuities that look very similar to vacancies as previously observed by Cervellon et al. [20] within the rough zone due to locally very high deformation magnitude (**Fig. 9 c** and **d**). These small pores whose size is below 1 µm may have also been inherited from the AM process.

**Fig. 10** shows the EBSD analysis performed just below the crack initiation site according to the localization provide in **Fig. 9a** by the green rectangle. The IQ+IPF images show that most of this region below the crack

initiation site presents angular variations lower than 1° indicating the absence of recrystallization. However, a small "recrystallization" zone of ≈ 60 µm in extension (see **Fig. 10d**) was observed close to the crack initiation zone. It is composed a several low angle boundaries of local misorientation typically lower than 10°. The internal stresses remaining from the melting lines combined with the HIP treatment can be the explanation of the recrystallized zone indicated in **Fig. 10**.

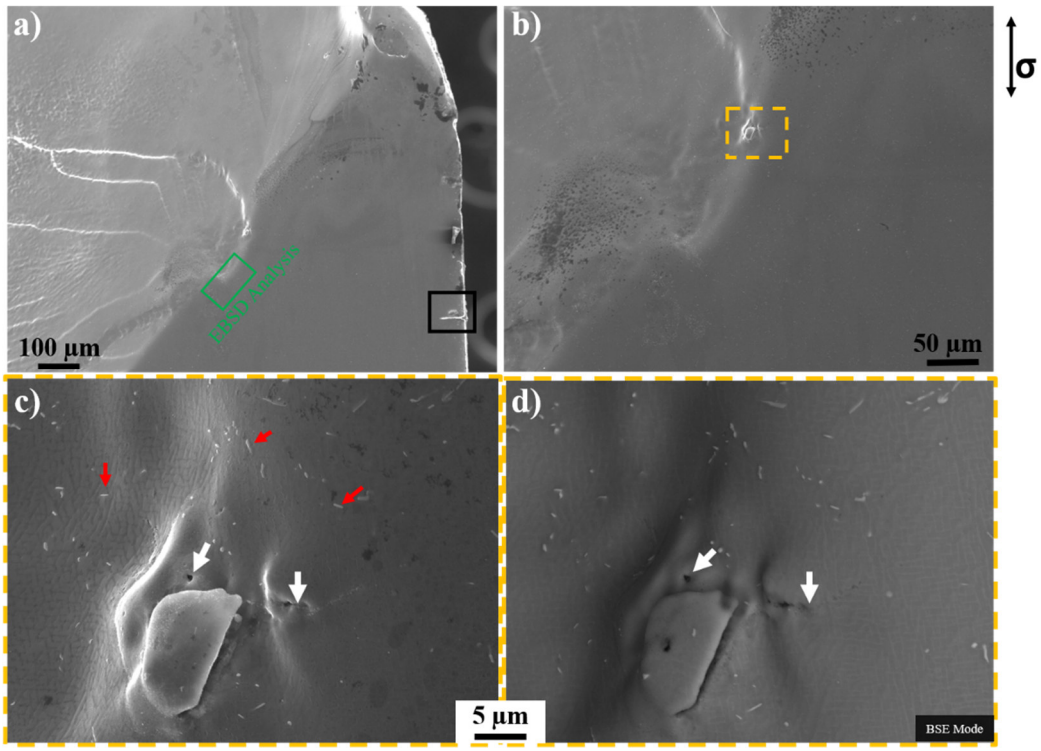


**Fig. 9.** (a) Crack initiation site of AM/HIP/REC-2 ($\sigma_a$ = 145 MPa, Nf = 4.9 × $10^9$ cycles) observed along a longitudinal section. Few secondary cracks are observed at the surface (see black square). (b) Crack initiation site identified by the rough zone, (c) magnification images using the SEI and (d) BSE imaging mode. White arrow is pointing out a remaining pore and red arrows highlight needle-shaped precipitates. The green square in (a) shows the location where the EBSD analyses have been performed. (For interpretation of the references to color in this figure legend, the reader is referred to the web version of this article.)

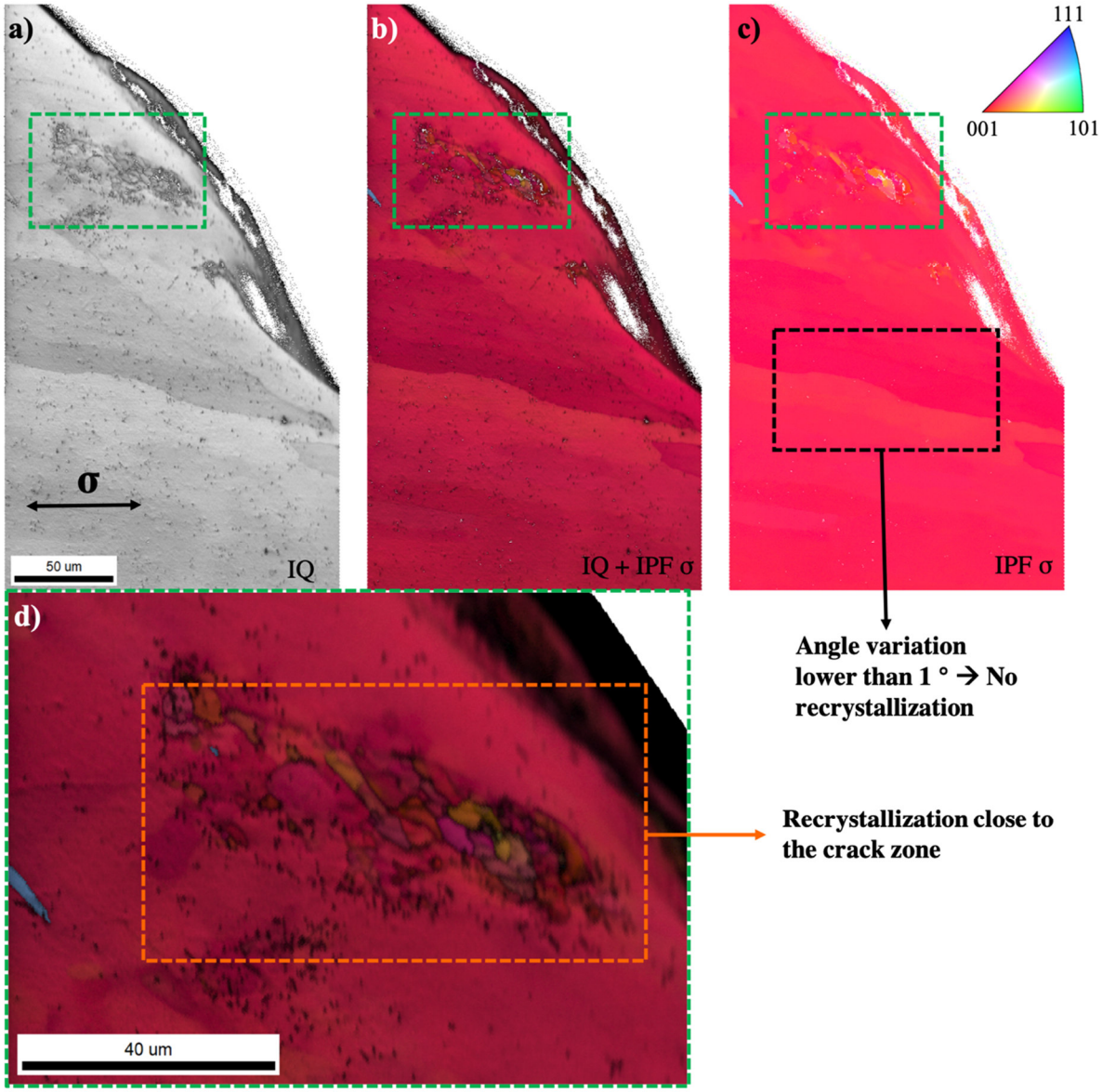


**Fig. 10.** EBSD characterization of AM/HIP/REC-2 ($\sigma_a$ = 145 MPa, Nf = 4.9 × $10^9$ cycles) crack initiation zone (green square in **Fig. 9a**) including (a) image quality (IQ). (b) IQ and inverse pole figure (IPF), (c) and IPF relative to the loading direction. Angle variation lower than 1° is pointed by the black dotted square. A region (dotted green rectangles in (a-c)) containing several recrystallized cells with low angle grain boundaries is shown in (d). (For interpretation of the references to color in this figure legend, the reader is referred to the web version of this article.)

### *3.2.2. Crack initiation from the surface: AM/HT/REC-1 specimen*

**Fig. 11** shows the features found along a longitudinal section of the AM/HT/REC-1 specimen. Failure from surface initiation is only shown for the HT sample since the results obtained for AM/HIP/REC-1, AM/HIP/FRS-2 and AM/HIP/FRS-3 (**Fig.6** and **Table 3**) are equivalent**. Fig. 11a** illustrates the presence of a secondary crack whose depth is ≈ 70 µm. This crack seems to be filled by oxides up to its tip. **Fig. 11b** and **c** are observations in BSE and SEI modes, respectively, allowing to highlight significant features like the square-like precipitates around the crack initiation zone and the oxidation inside the crack. A ≈ 30 µm-thick layer with Kirkendall porosity and precipitates

of different shapes appear underneath the surface (**Fig.11 d** and **e)**. **Fig. 11e** illustrates the oxides growing outwardly and leaving behind Kirkendall voids. None of these particular features were previously observed either in CMSX-4/Bridgman in VHCF at 1,000 °C by Cervellon et al. [15] or in the CMSX-4 PBF-E samples after LCF tests at 950 °C by Meid et al. [6], probably due to shorter duration of the tests.

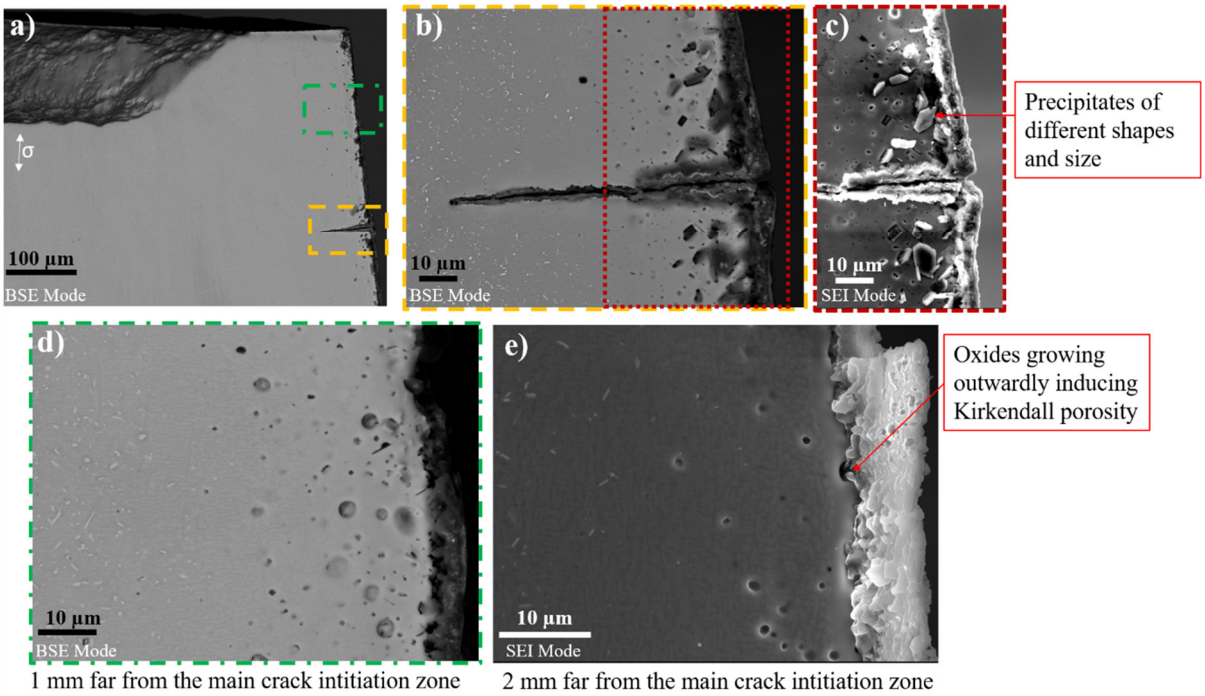


**Fig. 11.** Microstructure characterizations of AM/HT/REC-1 ($\sigma_a$ = 145 MPa, Nf = 3.2 × $10^{10}$ cycles) along a longitudinal section: (a) high magnification overview of one side of the sample in BSE mode. (b) Secondary crack detail (orange dotted rectangle in (a)) in BSE mode and (c) SEI mode. (d) Surface detail (green dotted rectangle in (a)) 1 mm far from the main crack initiation site in BSE mode, and (e) 2 mm far from the main crack initiation zone in SEI mode. (For interpretation of the references to color in this figure legend, the reader is referred to the web version of this article.)

**Fig. 12a** highlights the chemical elements that constitute the oxides and the precipitates. The external oxide scale outside the crack is mainly composed of O, Ni and Cr (light yellow and green). The internal crack oxides comprise Ti, Ta and Al (purple and dark pink). The needle-like precipitates are rich in Re (yellow) ≈ 20 wt. % (see also Re map in **Fig. 12b**), and several big precipitates are composed of Ta, W and Hf (red). The large square-shaped precipitates close to the surface are composed of N and Al (orange), and the small ones are composed of N and Ti (blue). Re-rich needle-shaped precipitates are probably TCP ones, presumably µ or P phases, based on their morphology and on their very high Re content [33].

The EDS composition profile of the oxide and the substrate is displayed in **Fig. 12b**. The oxide is divided in three main layers: an external NiO, an intermediate $Cr_2O_3$ and internal $Al_2O_3$ layers. Depletion of Al, Ta and Ti between the bulk and the surface is also observed (**Fig. 12c)**, which results in the countercurrent increase in Re and W.

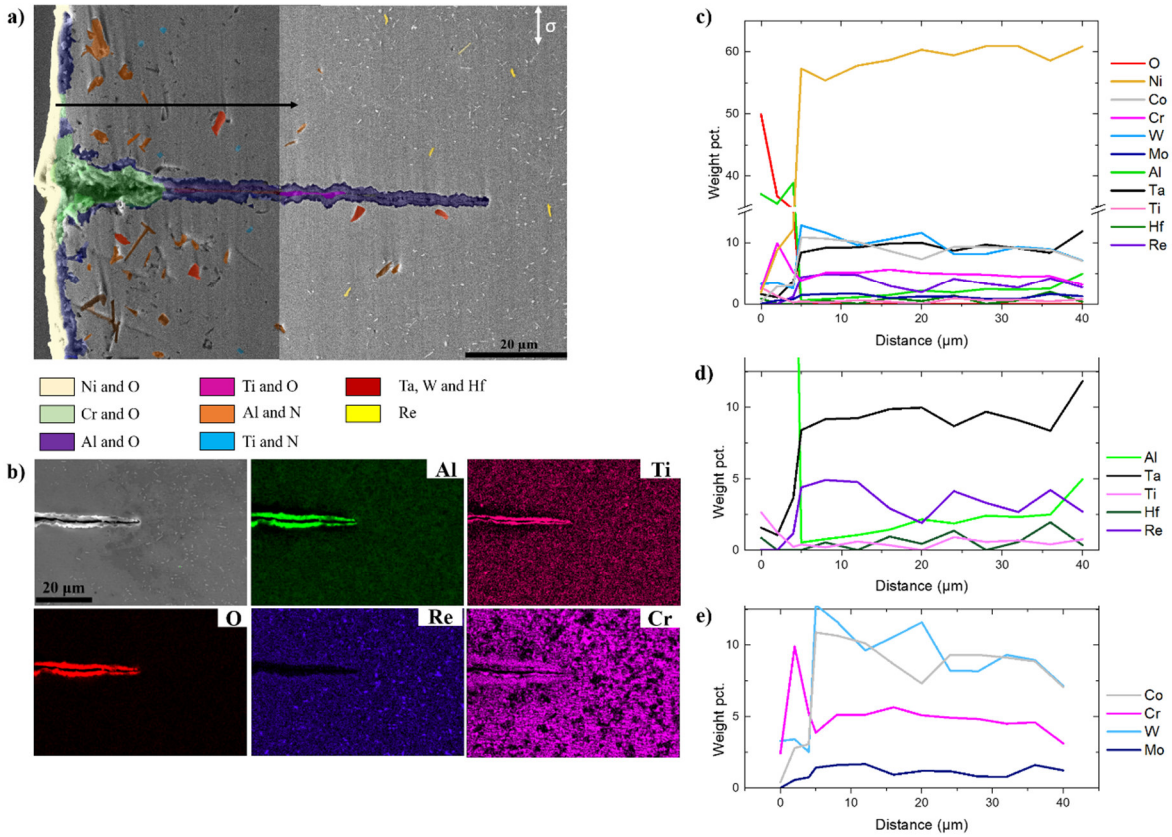


**Fig. 12.** AM/HT/REC-1 ($\sigma_a$ = 145 MPa, Nf = 3.2 × $10^{10}$ cycles) EDS analysis. (a) SEI image artificially colored with the Photoshop software in agreement with the chemical elements X-ray maps analysis in (b). (b) X-ray maps of the crack tip highlighting the elements O, Al, Re, Ti, and Cr. (c) Chemical composition through the profile illustrated by the black arrow in **Fig. 12a** including all elements, (d) with a focus on Al, Ta, Ti, Hf, and Re elements and (e) with a focus on Co, Cr, W, Mo elements. (For interpretation of the references to color in this figure legend, the reader is referred to the web version of this article.)

## 4. Discussion

From the present experiments, it has been observed that PBF-E processed specimens performed extremely well in VHCF at 1,000 °C/$R_\varepsilon$ = -1/f = 20 kHz provided that they are defect-free, i.e., they are fully single crystalline. Moreover, in comparison to conventionally processed (Bridgman solidification) Ni-based SX superalloys, which usually present crack initiation from the largest casting pores in these conditions irrespective of the alternating stress (see **Figs. 3** and **5** and refs. [14–20,23]), nearly all defect-free PBF-E processed specimens failed from the surface, with a crack initiation process assisted by oxidation (see **Figs. 3, 6, 7a, 8a, 11** and **12**) and equivalent results for fresh and recycled atomized powder. Since only AM specimens failed from an internal site, one can hypothesize on a very high dislocation density at local scale inherited from the building/HIP processes (**Fig. 9** and **10**). Yet, further analyses and additional results with a similar crack initiation mechanism would be required to unambiguously assess this potential mechanism of crack initiation. In the previous literature investigating fatigue properties of PBF-E-processed Ni-based SX superalloys, Meid et al. [6] compared the LCF life at 950 °C at a

stress ratio 0.6 of the AM SX with its parent cast material fully heat treated with and without HIP. They showed that the former performed better than the latter. In contrast, they did not report any failure related to the presence of grain boundaries probably because these stray grains were avoided by machining the samples from the center of bars. According to Meid's results [6] the crack initiation for PBF-E SX has three potential sources: (i) the interface of melting layers, (ii) the micro-porosity generated during solidification or, (iii) for the HIPed specimens, the precipitates formed at the location of collapsed pores. However, none of their specimens initiated or failed from the surface and we have to recall that the fatigue conditions used by Meid et al. introduced a pronounced cyclic ratcheting, i.e. creep strongly contributed to the damage mechanisms [6].

The following discussion will hence focus on the VHCF damage mechanisms of PBF-E-processed specimens, with a special focus on the crack initiation mechanism from the surface assisted by oxidation.

### *4.1. Crack initiation at grain boundaries*

According to **Fig. 3** and **Table 3**, the presence of stray grains within the gauge part of VHCF specimens induces a spectacular debit in fatigue life. Six specimens even failed during the initial ramping-up in alternating stress (see **Fig. 4**). These grains are either inherited from the PBF-E building process (i.e., the polycrystalline shell as shown in **Fig. 1a** could have been deeper in some AM processed specimens leading to the presence of grains within the gauge part of specimens after machining/polishing) and/or the HIPing process. While (surface) recrystallization is known to decrease the LCF life of Ni-based single crystalline superalloys [34,35], no prior study reported on the consequence of stray grain on the VHCF life at high temperature of Ni-based SX superalloys, according to the authors' best knowledge. We may only mention that a directionally solidified alloy (DS200+Hf), presenting several ≈ <001> columnar grains within the gauge part of VHCF specimens (i.e. low angle grain boundaries with respect to the loading direction [36]), performs slightly worse in VHCF at 1,000 °C/$R_\varepsilon$ = -1/f = 20 kHz compared to SX specimens solidified with the same casting parameters [15]. Hence, highly misoriented grains from the perfect [001] crystallographic orientation is critical to the VHCF life. In fact, as VHCF specimens used in the present study are designed so as to obtain a frequency of resonance in tension/compression of 20 kHz +/- 500 Hz [32], such recrystallized grains have a Young's modulus far higher than the one along the <001> orientation (i.e. 93 GPa for CMSX-4/Bridgman). Hence, the local frequency of resonance is far different from 20 kHz leading to a local stress concentration at grain boundaries. Failure in shear mode at the grain boundary is obtained in such a condition. The analysis of the role of recrystallized grains on the VHCF life of Ni-based SX superalloy specimens will be analyzed in greater details in a forthcoming article, by using finite element simulations and bicrystalline specimens tested in VHCF in the same condition.

### *4.2. Microstructure evolution*

PBF-E specimens that failed through cracks whose nucleation/micropropagation is assisted by oxidation presented a very high VHCF life (between 70 and 447 h) at 1,000 °C. According to **Figs. 11** and **12**, these specimens presented very different intermetallic precipitates in addition to the usual γ′ precipitates. AM/HT/REC and AM/HIP/REC coupons were then overaged in isothermal conditions for 480 h at 1,000 °C to compare the microstructure evolutions with and without ultrasonic fatigue loading. Such a comparison is shown in **Fig.13**.

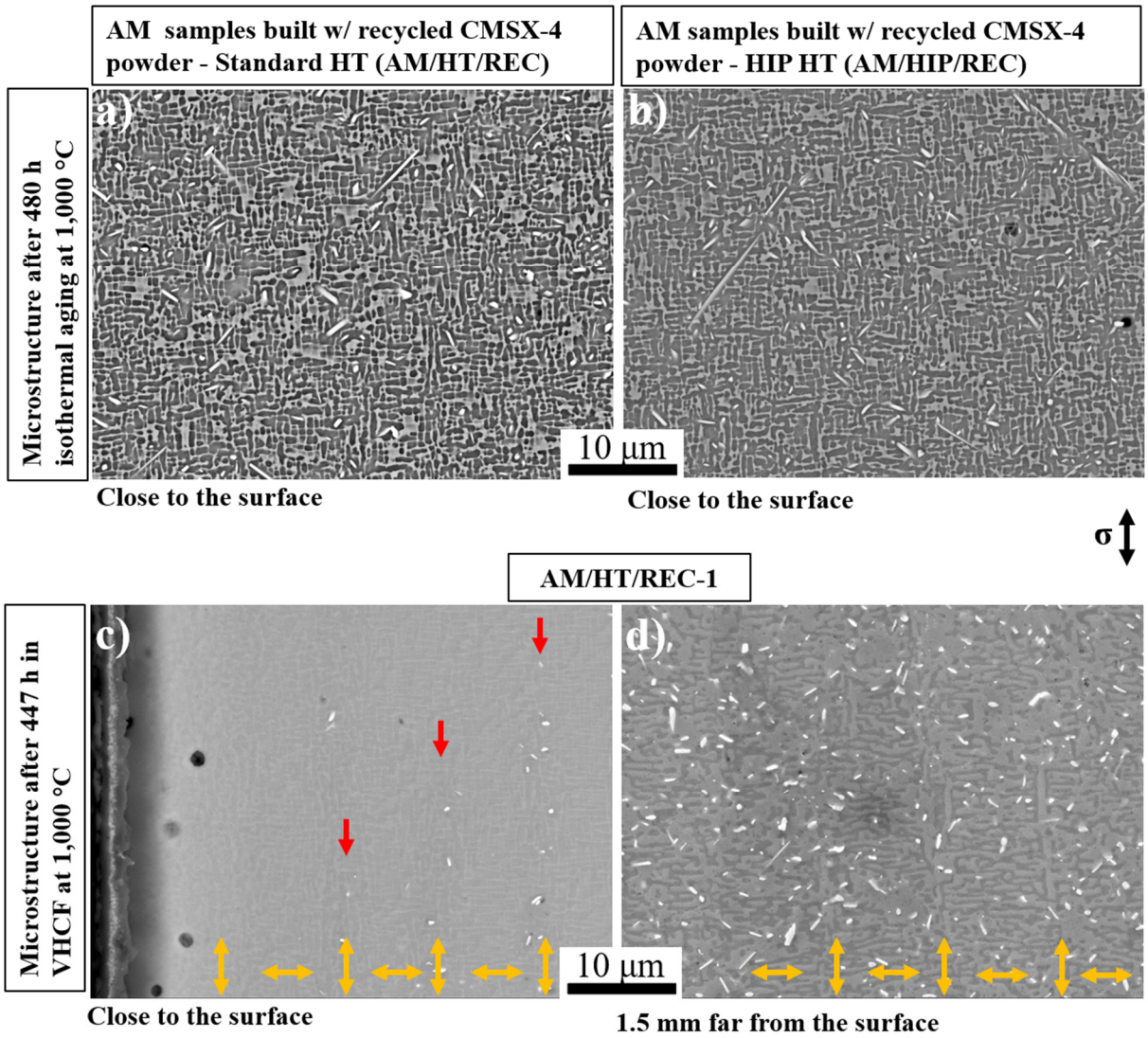


**Fig. 13.** (a) Microstructure evolution after 480 h at 1,000 °C for AM/HT/REC and (b) AM/HIP/REC. Both microstructures were taken 0.5 mm below the fracture surface. (c) Microstructure evolution after ≈ 447 h in VHCF at 1,000 °C for AM/HT/REC-1 ($\sigma_a$ = 145 MPa, Nf = 3.2 × $10^{10}$ cycles) close to the surface and (d) 1.5 mm below the surface. Red arrows are showing TCP precipitates along the dendritic zones. Yellow arrows are showing the directions of local γ' coarsening. (For interpretation of the references to color in this figure legend, the reader is referred to the web version of this article.)

At 1,000 °C, the superalloy CMSX-4/Bridgman is known to be prone to topologically close-packed (TCP) precipitates [14,37–40] that are well known to lower the mechanical properties [41,42]. This TCP precipitation is also known to be enhanced at high temperature by the introduction of pre-deformation [43,44] or by the very high local plastic deformation in the rough zone close to stress raisers in VHCF [20]. As already investigated by Pistor et al. [30], TCP phases precipitate in PBF-E CMSX-4 alloy at high temperatures (around 1,050°C) and for longtime exposures. In our study, based on the morphology and EDS analysis showing a very high Re content shown in **Fig. 12**, we believe that needle-type precipitates are also TCP phases [39]. Moreover, AM/HT/REC-1 test lasted ≈ 447

h, i.e. long enough to be in the precipitation domain of TCP phases at high temperatures according to previous literature [33,38,39], as opposed to the tests performed by Meid et al. [9] that only lasted 48 h in LCF.

Such TCP phases precipitate homogeneously (≈ 1 % in area fraction) in the material without loading (**Figs. 13a** and **b**). Comparing **Fig. 13d** (2.5 % in area fraction) with **Figs. 13a** and **b**, imposing the VHCF loading does not seem to deeply affect the overall amount of TCP phases, but their location varies close to the surface, where they seem to mainly precipitate in former primary dendrite arms (red arrows at **Fig. 13c**). Further, their density increases from the surface towards the bulk. This can be explained by the local change in chemical composition due to the depletion of the other alloying elements to form the oxides, especially Cr and W known to favor TCP precipitation in CMSX-4/Bridgman [33], in addition to Re. This result is also in good agreement with the Re distribution map of **Fig. 12b** showing almost no TCP precipitates close to the crack tip.

The square-type precipitates rich in N are the nitrides developed close to the surface due to the low oxygen pressure. As the oxygen is being consumed by the Ni, Al, and Cr elements to form the oxide layer, the oxygen pressure locally drops, and the 78 % of $N_2$ present in the air diffuses in the substrate reacting with Al and Ti. Nitrides are known to be brittle structures, decreasing the mechanical properties of superalloys, especially in fatigue at low temperatures [45–47]. The Ta/W/Hf-rich carbides previously observed in MAR-M247 [48] and in Mar-M200+Hf/DS200+Hf [49] are also known to favor crack initiation in LCF [50]

The voids appearing just beneath the oxide layer (**Figs. 11 b-e)** have been previously observed after the high temperature oxidation of various Ni-based superalloys [51–54] and are related to the vacancy supersaturation according to Evans et al. [55]. Such vacancies originate by the major outward cation diffusion and the countercurrent injection of vacancies into the bulk resulting in the well-known Kirkendall porosity [56]. One shall notice that the Kirkendall porosity often driven by the gradient of chemical potential [57] (**Fig. 12c**) was not observed in the absence of mechanical loading. This finding suggests that greater outward diffusion was most likely enhanced through the dislocations introduced upon the VHCF [58] allowing to reach voids of ≈ 5 μm diameter. One may also speculate on the high dislocations' density inherited from the very PBF-E additive manufacturing process that can also foster oxidation. Indeed, it is known that a very high dislocation density is present within the material after the PBF-E process [59], and this was also confirmed by the fact it has been impossible to conduct VHCF tests in the present conditions at alternating stresses greater than 180 MPa (see Fig. 2), due to a too pronounced self-heating. Regarding oxidation, Juillet et al. demonstrated that the instantaneous parabolic rate ($k_p$) constants could not be calculated in an AM IN-718 superalloy due to enhanced growth of the oxides in comparison with the forged counterparts and related this to the significantly higher density of internal defects assessed by transmission electron microscopy (TEM) [60]. As a result, the selective outward diffusion of the most oxidizable elements to form the oxide scale brings about the precipitation of the strong carbide and nitride formers underneath [61].

### *4.3. Crack initiation and propagation mechanism assisted by oxidation*

This is the first time that a VHCF life controlled by oxidation is presented in the open literature for a Ni-based SX superalloy at high temperature in fully reversed conditions, and in the absence of any surface recrystallization mechanisms. In fact, several EBSD maps have been performed in this work for specimens showing surface crack

initiation and no evidence of recrystallization close to secondary cracks in PBF-E processed specimens has been observed (see, e.g., Fig. 14). Cervellon already observed that surface cracks may develop in fully reversed conditions at the same temperature for long VHCF tests [15,17], but the main crack initiation (almost) always occurred at an internal site (a casting pore). Our present results are somehow different from previous examples of fatal crack initiation from the surface in VHCF in this class of alloys showing the presence of recrystallized grains (associated or not to a coating deposition process) [21,22] or from a stress concentration at the surface of specimens, due to a prior plastic deformation before testing specimens in VHCF at 1,000°C/R=0.5/f = 20 kHz [23].

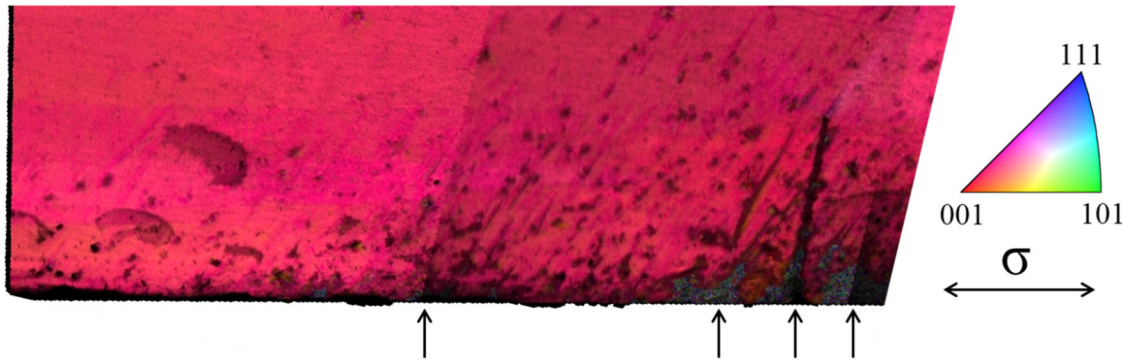


**Fig. 14.** EBSD characterization of AM/HT/REC-1 ($\sigma_a$ = 145 MPa, Nf = 3.2 × $10^{10}$ cycles) close to surface secondary cracks. The Index Quality map is superimposed to the inverse pole figure (IPF) relative to the loading direction. Black arrows indicate secondary cracks initiated from the surface.

**Fig. 15** presents the typical crack initiation mechanism as understood from the microstructures and chemical analyses shown before. Starting from the initial optimized γ/γ' microstructure (**Fig. 15a**) that likely contains intrinsic processing defects (incl. a high dislocation density), oxidation rapidly occurs at the specimens' surface, leading to a rougher surface and to the depletion of (mostly) Al and Cr and the subsequent precipitation of nitrides and carbides below the surface (**Fig. 15b**). Dislocation climbing may be then fostered with the VHCF loading, results in enhanced outward cation diffusion and the derived formation of Kirkendall voids just below the free surface (**Fig. 15c**). Increasing the duration of VHCF exposure at high temperature leads to TCP precipitation and to non-directional coarsening of γ' precipitates (see **Fig. 15c**), resulting from a small remaining dendritic segregation, as already proposed by Hazotte et al. [62]. Overall, the subsurface layer is composed of voids, a γ matrix depleted from its main refractory elements filled with quite brittle particles (nitrides, carbides). The increased surface roughness due to oxidation combined with the presence these voids/non-metallic inclusions lead to a surface crack initiation at a void or a non-metallic particle. This micro-crack then propagates in mode I through the microstructure, assisted by oxidation, up to failure (**Figs. 15d** and **e**).

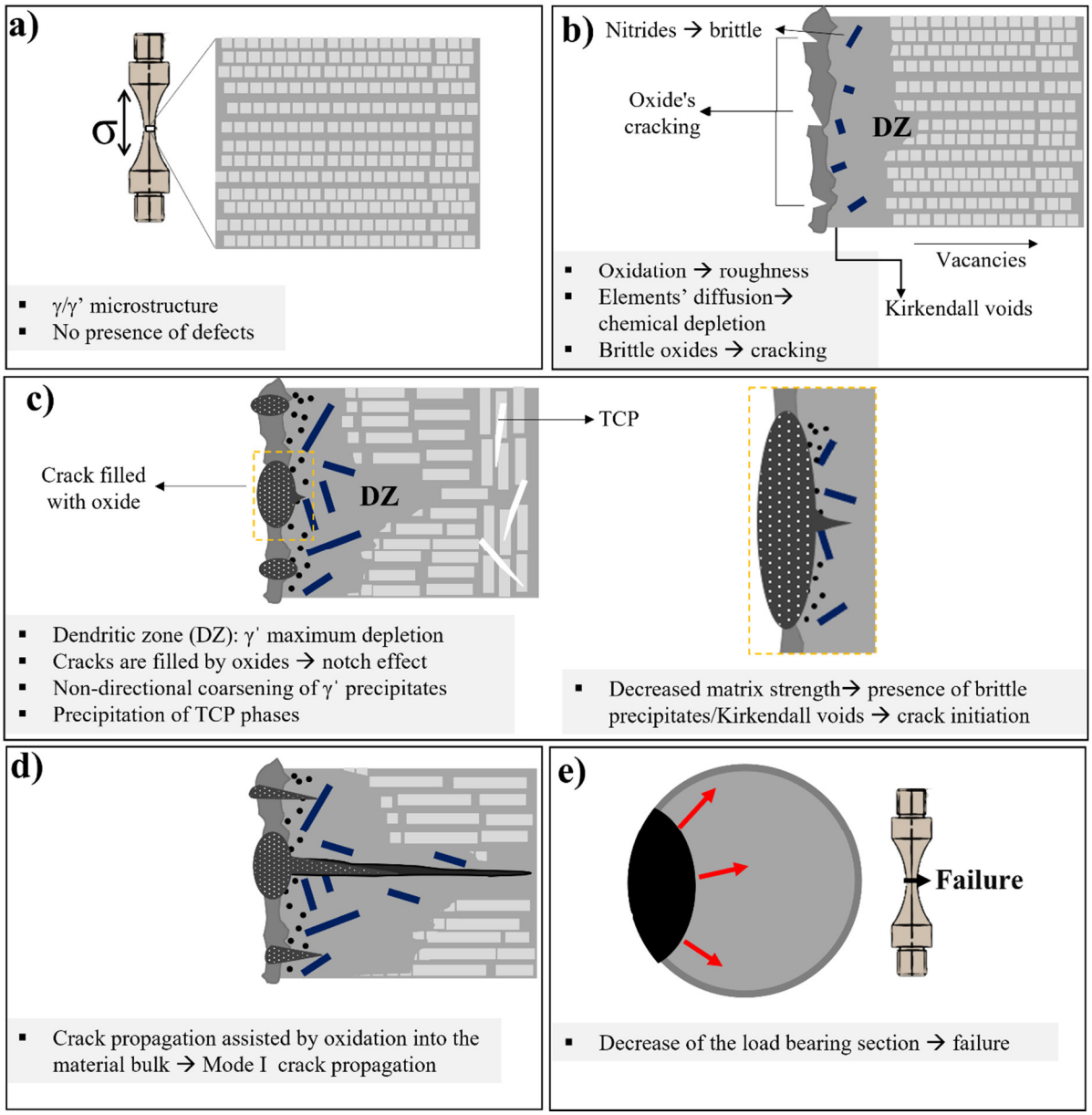


**Fig. 15.** Schematic illustration of the oxidation-controlled crack initiation mechanism of PBF-E CMSX-4 SX Ni-based superalloys in VHCF conditions at 1,000 °C/$R_\varepsilon$ = -1/f = 20 kHz. (a) The initial optimized γ/γ' microstructure is oxidized leading to the precipitation of nitrides (b) and carbides below the surface and simultaneously developing a rougher surface. (c) Subsequently the oxidation leads to the formation of Kirkendall voids just below the free surface, followed by the precipitation of TCP phases as well as non-directional coarsening of γ' precipitates. The increased surface roughness due to oxidation combined with the presence these voids/non-metallic inclusions lead to a surface crack initiation at a void or a non-metallic particle. (d) The micro-crack then propagates in mode I through the microstructure, assisted by oxidation, up to failure (e). (For interpretation of the references to color in this figure legend, the reader is referred to the web version of this article.)

From the present investigation, it has been shown that provided PBF-E processed CMSX-4 specimens are defect-free (i.e., no stray grain within the gauge part of specimens), a very high VHCF life is obtained, comparable or

even longer than the one obtained for conventionally processed Ni-based SX superalloys. A S-N diagram at 1,000 °C/$R_\varepsilon$ = -1/f = 20 kHz including defect-free PBF-E processed CMSX-4 specimens and several other results obtained for conventionally processed Ni-based SX superalloys with an internal crack initiation at a solidification pore is shown in the **Fig. 16**. It is important to point out that the results from the internal database in Institut Pprime/ISAE-ENSMA (France) have been obtained using "legacy" Ni-based SX superalloys such as Rene N5 and AM1 [63] and but also newer generations such as CMSX-4 Plus, DD33, TMS-238, MC-NG, and TROPEA [18,19,63]. Their chemical composition is given in **Table 4**. Further, they were solidified using a Bridgman or an LMC process. According to **Fig. 16**, an environmental VHCF limit under such conditions can clearly be identified, towards the highest VHCF lives. Up to now, most of the authors focused their investigations on VHCF damage mechanisms from either casting pores or from non-metallic inclusions (TCP phases, eutectics, carbides…), i.e. from process related "defects" [15,19,20,57,64]. When nearly all such defects are removed from the material, and provided that a good surface preparation of specimens is performed to avoid any surface recrystallization due to too large residual stresses known to be detrimental the fatigue life [34,35], the intrinsic VHCF life is controlled by the alloy's chemistry. In such conditions, the VHCF life of single crystalline Ni-based superalloys is hence controlled by the environmental resistance of the alloy, i.e., by its own chemistry and the overall microstructure of the alloys. The present study also suggests that no fatigue limit exists in these fatigue conditions at high temperature, but such a question should also be investigated at higher and lower temperatures to get a better picture of oxidation controlled VHCF crack initiation mechanisms.

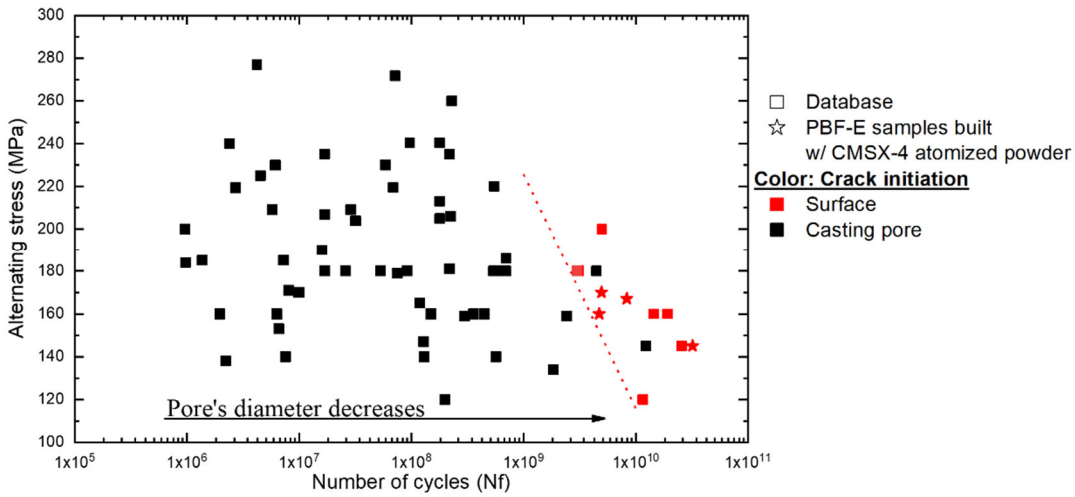


**Fig. 16.** S-N diagram at 1,000 °C, $R_\varepsilon$ = -1 / f = 20 kHz including defect-free PBF-E processed CMSX-4 SX specimens and other "conventionally" processed SX specimens made of Rene N5, AM1, CMSX-4 Plus, DD33, TMS-238, MC-NG and TROPEA alloys with different solidification parameters [18,19,63]. The alternating stress $\sigma_a$ is plotted as a function of the number of cycles to failure. A transition from an internal crack initiation site at a large casting pore to the surface is illustrated. (For interpretation of the references to color in this figure legend, the reader is referred to the web version of this article.)

**Table 4**

Chemical composition (in wt. pct) of AM1, Rene N5, CMSX-4 Plus, DD33, TMS-238, MC-NG and TROPEA alloys

| Alloy | Ni | Cr | Mo | Co | W | Al | Ti | Ta | Hf | Re | Others |
|---|---|---|---|---|---|---|---|---|---|---|---|
| **AM1** | Bal. | 7.5 | 2.0 | 6.6 | 5.5 | 5.2 | 1.2 | 7.9 | 0.1 | | |
| **Rene N5** | Bal. | 7.0 | 2.0 | 8.0 | 5.0 | 6.2 | | 7.0 | 0.2 | 3.0 | |
| **CMSX-4 Plus** | Bal. | 3.5 | 0.6 | 10.0 | 6.0 | 5.7 | 0.9 | 8.0 | 0.1 | 4.8 | |
| **DD33** [65] | Bal. | 3.0 | 1.0 | 12.0 | 6.0 | 6.0 | | 8.0 | 0.1 | 4.0 | |
| **TMS-238** [66] | Bal. | 4.6 | 1.1 | 6.5 | 4.0 | 5.9 | | 7.6 | 0.1 | 6.4 | 5.0 Ru |
| **MCNG** [67] | Bal. | 4.0 | 1.0 | <0.2 | 5.0 | 6.0 | 0.5 | 5.0 | 0.1 | 4.0 | 4.0 Ru |
| **TROPEA** [68] | Bal. | 6.4 | 0.6 | 8.9 | 6.1 | 5.4 | 1.0 | 9.1 | 0.08 | 1.0 | 1.95 Pt |

## 5. Conclusions

Very high cycle fatigue performances and crack initiation mechanisms at high temperature of PBF-E CMSX-4 SX Ni-based superalloy have been investigated under fully reversed conditions ($R_\varepsilon$ = -1), f = 20 kHz and 1,000 °C. Comparisons have been made with conventionally processed Ni-based SX superalloys of ERBO/1 and CMSX-4/Bridgman type. The following main conclusions have been obtained:

- All Bridgman processed specimens failed from an internal casting pore site.
- The VHCF lifetime of PBF-E processed specimens in these conditions is comparable or higher than the one of Bridgman solidified Ni-based SX superalloys provided that no defect (e.g., stray grain) is present within the gauge part of the specimens.
- The presence of high angle grain boundaries/stray grains leads to a spectacular (more than 3 decades) decrease in VHCF lifetime compared to defect-free specimens.
- Due to the absence of large casting pores/non-metallic inclusions, nearly all defect-free PBF-E processed specimens failed by an oxidation assisted surface crack initiation process. Hence, the superalloy chemistry and microstructure stability below the surface controls the crack initiation and first stages of propagation and an environmentally controlled VHCF life limit has been identified in these conditions.

**Acknowledgements**

The authors wish to thank Florence Hamon, Florent Mauget and Jacques Lefort (Physics and Mechanics of Materials Department, Institut Pprime, France) for their help and advice during mechanical testing and microstructural observations. Institut Pprime gratefully acknowledges “Contrat de Plan Etat - Région Nouvelle-Aquitaine (CPER)” as well as the “Fonds Européen de Développement Régional (FEDER)” for their financial support to the reported work. Part of this study was supported by the Nouvelle-Aquitaine French region through the ECOREVE project (project number 2018-1R10122). This study is also part of the "Self-Heating" ANR-Safran-Naval group research chair (Grant # ANR-20-CHIN-0002) involving the Safran Companies, Naval group, ENSTA Bretagne (IRDL) and Institut Pprime. F. Pedraza gratefully acknowledges the CNRS for funding his secondment period at Institut Pprime. Institute of Metal Research, Shenyang, P.R. China (Pr. J. Zhang) and Safran Aircraft Engines are acknowledged for providing DD33 and AM1/Rene N5 materials used in the final discussion, respectively. The authors acknowledge funding by the Deutsche Forschungsgemeinschaft (DFG) in the framework of the collaborative research center SFB/TR 103 through projects B2 (JP, CK) and T4 (ILG, BR, WT).

**References**

[1] R.C. Reed, The superalloys - Fundamentals and applications, First edit, Cambridge University Press, Cambridge, 2006.

[2] T.M. Pollock, S. Tin, Nickel-Based Superalloys for Advanced Turbine Engines: Chemistry, Microstructure and Properties, J. Propuls. Power. 22 (2008) 361–374.

[3] P. Caron, T. Khan, Evolution of Ni-based superalloys for single crystal gas turbine blade applications, Aerosp. Sci. Technol. 3 (1999) 513–523.

[4] M. Perrut, P. Caron, M. Thomas, A. Couret, High temperature materials for aerospace applications: Ni-based superalloys and γ-TiAl alloys, Comptes Rendus Phys. 19 (2018) 657–671.

[5] E. Chauvet, C. Tassin, J.J. Blandin, R. Dendievel, G. Martin, Producing Ni-base superalloys single crystal by selective electron beam melting, Scr. Mater. 152 (2018) 15–19.

[6] C. Körner, M. Ramsperger, C. Meid, D. Bürger, P. Wollgramm, M. Bartsch, G. Eggeler, Microstructure and Mechanical Properties of CMSX-4 Single Crystals Prepared by Additive Manufacturing, Metall. Mater. Trans. A Phys. Metall. Mater. Sci. 49 (2018) 3781–3792.

[7] K. Harris, G.L. Erickson, S.L. Sikkenga, W.D. Brentnall, J.M. Aurrecoechea, K.G. Kubarych, Development of two rhenium- containing superalloys for single- crystal blade and directionally solidified vane applications in advanced turbine engines, in: Superalloys 1992, 1992: pp. 297–306.

[8] K. Harris, J.B. Wahl, Improved single crystal superalloys, CMSX-4®(SLS)[La+Y] and CMSX-486®, Proc. Int. Symp. Superalloys. (2004) 45–52.

[9] C. Meid, A. Dennstedt, M. Ramsperger, J. Pistor, B. Ruttert, I. Lopez-Galilea, W. Theisen, C. Körner, M. Bartsch, Effect of heat treatment on the high temperature fatigue life of single crystalline nickel base superalloy additively manufactured by means of selective electron beam melting, Scr. Mater. 168 (2019)

124–128.

[10] P. Caron, T. Khan, Improvement of creep strength in a nickel-based single-crystal superalloy by heat treatment, Mater. Sci. Eng. 61 (1983) 173–184.

[11] B.C. Wilson, J.A. Hickman, G.E. Fuchs, The effect of solution heat treatment on a single-crystal Ni-based superalloy, JOM - Res. Summ. 55 (2003) 35–40.

[12] Transregio, (n.d.). https://www.sfb-transregio103.de.

[13] W.J. Zhang, Thermal mechanical fatigue of single crystal superalloys: Achievements and challenges, Mater. Sci. Eng. A. 650 (2016) 389–395.

[14] J.Z. Yi, C.J. Torbet, Q. Feng, T.M. Pollock, J.W. Jones, Ultrasonic fatigue of a single crystal Ni-base superalloy at 1000 °C, Mater. Sci. Eng. A. 443 (2007) 142–149.

[15] A. Cervellon, J. Cormier, F. Mauget, Z. Hervier, Y. Nadot, Very high cycle fatigue of Ni-based single crystal superalloys at high temperature, Metall. Mater. Trans. A. 49 (2018) 3938–3950.

[16] A. Cervellon, J.Z. Yi, F. Corpace, Z. Hervier, J. Rigney, P.K. Wright, C.J. Torbet, J. Cormier, J.W. Jones, T.M. Pollock, Creep, fatigue, and oxidation interactions during High and very high cycle fatigue at elevated temperature of nickel-base single crystal superalloys, in: S. Tin, M. Hardy, J. Clews, J. Cormier, Q. Feng, J. Marcin, C. O'brien, A. Suzuki (Eds.), Proc. Int. Symp. Superalloys 2020, Springer US, Seven Springs, PA, USA, 2020: pp. 185–195.

[17] A. Cervellon, J. Cormier, F. Mauget, Z. Hervier, VHCF life evolution after microstructure degradation of a Ni-based single crystal superalloy, Int. J. Fatigue. 104 (2017) 251–262.

[18] L.M. Bortoluci, S. Utada, J. Rame, L. Mataveli Suave, K. Kawagishi, H. Harada, P. Villechaise, J. Cormier, Tensile, Low Cycle Fatigue, and Very High Cycle Fatigue characterizations of advanced single crystal Nickel-based superalloys, in: S. Tin, M. Hardy, J. Clews, J. Cormier, Q. Feng, J. Marcin, C. O'brien, A. Suzuki (Eds.), Proc. Int. Symp. Superalloys 2020, Springer US, Seven Springs, PA, USA, 2020: pp. 341–351.

[19] L.M. Bortoluci, L. Mataveli Suave, A. Cervellon, P. Villechaise, J. Cormier, LCF, HCF and VHCF life sensitivity to solution heat treatment of a third-generation Ni-based single crystal superalloy, Int. J. Fatigue. 130 (2020) 105247.

[20] A. Cervellon, S. Hemery, P. Kürnsteiner, B. Gault, P. Kontis, J. Cormier, Crack initiation mechanism during very high cycle fatigue of Ni-based single crystal superalloys at high temperature, Acta Mater. 188 (2020) 131–144.

[21] A. Cervellon, L.M. Bortoluci Ormastroni, Z. Hervier, T.M. Pollock, F. Pedraza, J. Cormier, Damage mechanisms during very high cycle fatigue of a coated and grit-blasted Ni-based single-crystal superalloy, Int. J. Fatigue. 142 (2021) 105962.

[22] Z. Zhao, Q. Li, F. Zhang, W. Xu, B. Chen, Transition from internal to surface crack initation of a single-crystal superalloys in the very-high-cycle fatigue regime at 1100 °C, Int. J. Fatigue. 150 (2021) 106343.

[23] S. Utada, L.M. Bortoluci, J. Rame, P. Villechaise, J. Cormier, VHCF life of AM1 Ni-based single crystal

superalloy after pre-deformation, Int. J. Fatigue. 148 (2021) 106224.

[24] I. Lopez-Galilea, B. Ruttert, J. He, T. Hammerschmidt, R. Drautz, B. Gault, W. Theisen, Additive manufacturing of CMSX-4 Ni-base superalloy by selective laser melting: Influence of processing parameters and heat treatment, Addit. Manuf. 30 (2019) 100874.

[25] B. Ruttert, M. Ramsperger, L. Mujica Roncery, I. Lopez-Galilea, C. Körner, W. Theisen, Impact of hot isostatic pressing on microstructures of CMSX-4 Ni-base superalloy fabricated by selective electron beam melting, Mater. Des. 110 (2016) 720–727.

[26] L. Mujica Roncery, I. Lopez-Galilea, B. Ruttert, S. Huth, W. Theisen, Influence of temperature, pressure, and cooling rate during hot isostatic pressing on the microstructure of an SX Ni-base superalloy, Mater. Des. 97 (2016) 544–552.

[27] A.B. Parsa, P. Wollgramm, H. Buck, C. Somsen, A. Kostka, I. Povstugar, P.P. Choi, D. Raabe, A. Dlouhy, J. Müller, E. Spiecker, K. Demtroder, J. Schreuer, K. Neuking, G. Eggeler, Advanced scale bridging microstructure analysis of single crystal Ni-base superalloys, Adv. Eng. Mater. 17 (2015) 216–230.

[28] E. Plancher, P. Gravier, E. Chauvet, J.J. Blandin, E. Boller, G. Martin, L. Salvo, P. Lhuissier, Tracking pores during solidification of a Ni-based superalloy using 4D synchrotron microtomography, Acta Mater. 181 (2019) 1–9.

[29] M. Ramsperger, L. Mújica Roncery, I. Lopez-Galilea, R.F. Singer, W. Theisen, C. Körner, Solution Heat Treatment of the Single Crystal Nickel-Base Superalloy CMSX-4 Fabricated by Selective Electron Beam Melting, Adv. Eng. Mater. 17 (2015) 1486–1493.

[30] J. Pistor, C. Körner, Formation of topologically closed packed phases within CMSX-4 single crystals produced by additive manufacturing, Mater. Lett. X. 1 (2019) 1–4.

[31] M. Ramsperger, R.F. Singer, C. Körner, Microstructure of the Nickel-Base Superalloy CMSX-4 Fabricated by Selective Electron Beam Melting, Metall. Mater. Trans. A Phys. Metall. Mater. Sci. 47 (2016) 1469–1480.

[32] A. Cervellon, Propriétés en fatigue à grand et très grand nombre de cycles et à haute température des superalliages base nickel monogranulaires, PhD Thesis - Ecole Nationale Superieure de Mecanique et d'Aerotechnique (ISAE-ENSMA), France, 2018. https://tel.archives-ouvertes.fr/tel-01940424/document.

[33] B. Dubiel, P. Indyka, I. Kalemba-Rec, A. Kruk, T. Moskalewicz, A. Radziszewska, S. Kąc, A. Kopia, K. Berent, M. Gajewska, The influence of high temperature annealing and creep on the microstructure and chemical element distribution in the γ, γ′ and TCP phases in single crystal Ni-base superalloy, J. Alloys Compd. 731 (2018) 693–703.

[34] X. Ma, H.J. Shi, J. Gu, Z. Yang, G. Chen, O. Luesebrink, H. Harders, Influence of surface recrystallization on the low cycle fatigue behaviour of a single crystal superalloy, Fatigue Fract. Eng. Mater. Struct. 38 (2015) 340–351.

[35] X. Ma, J. Jiang, W. Zhang, H.J. Shi, J. Gu, Effect of local recrystallized grains on the low cycle fatigue behavior of a nickel-based single crystal superalloy, Crystals. 9 (2019) 312.

[36] L. Mataveli Suave, J. Cormier, P. Villechaise, D. Bertheau, G. Benoit, F. Mauget, G. Cailletaud, L. Marcin, High Temperature Creep Damage Mechanisms in a Directionally Solidified Alloy: Impact of Crystallography and Environment, in: M.C. Hardy, E. Huron, U. Glatzel, B. Griffin, B. Lewis, C.M.F. Rae, V. Seetharaman, S. Tin (Eds.), Proc. Int. Symp. Superalloys, TMS (The Minerals, Metals & Materials Society), Seven Springs, 2016: pp. 747–756.

[37] R. Giraud, Influence de l'histoire thermique sur les propriétés mécaniques à haute et très haute température du superalliage monocristallin CMSX-4®, PhD Thesis - Ecole Nationale Superieure de Mecanique et d'Aerotechnique (ISAE-ENSMA), France, 2014. https://www.theses.fr/2014ESMA0005.

[38] K. Cheng, C. Jo, T. Jin, Z. Hu, Precipitation behavior of μ phase and creep rupture in single crystal superalloy CMSX-4, J. Alloys Compd. 509 (2011) 7078–7086.

[39] C.M.F. Rae, R.C. Reed, The precipitation of topologically close-packed phases in rhenium-containing superalloys, Acta Mater. 49 (2001) 4113–4125.

[40] I. Lopez-Galilea, J. Koßmann, A. Kostka, R. Drautz, L. Mujica Roncery, T. Hammerschmidt, S. Huth, W. Theisen, The thermal stability of topologically close-packed phases in the single-crystal Ni-base superalloy ERBO/1, J. Mater. Sci. 51 (2016) 2653–2664.

[41] J.B. le Graverend, J. Cormier, S. Kruch, F. Gallerneau, J. Mendez, Microstructural parameters controlling high-temperature creep life of the nickel-base single-crystal superalloy MC2, Metall. Mater. Trans. A Phys. Metall. Mater. Sci. 43 (2012) 3988–3997.

[42] M. Simonetti, P. Caron, Role and behaviour of μ phase during deformation of a nickel-based single crystal superalloy, Mater. Sci. Eng. A. 254 (1998) 1–12.

[43] C. Meid, M. Eggeler, P. Watermeyer, A. Kostka, T. Hammerschmidt, R. Drautz, G. Eggeler, M. Bartsch, Stress-induced formation of TCP phases during high temperature low cycle fatigue loading of the single-crystal Ni-base superalloy ERBO/1, Acta Mater. 168 (2019) 343–352.

[44] B.G. Choi, C.Y. Jo, H.U. Hong, I.S. Kim, S.M. Seo, H.M. Kim, Effect of pre-strain on microstructural evolution during thermal exposure of single crystal superalloy CMSX-4, Trans. Nonferrous Met. Soc. China (English Ed. 21 (2011) 1291–1296.

[45] A. Govaere, A.-L. Rouffie, J.M. Franchet, D. Galy, C. Dumont, A. Devaux, C. Crozet, P. Kontis, P. Villechaise, J. Cormier, Is the Carbon Content Really an Issue for the LCF Durability of Forged γ/γ′ Ni-Based Disk Alloys?, in: S. Tin, M. Hardy, J. Clews, J. Cormier, Q. Feng, J. Marcin, C. O'brien, A. Suzuki (Eds.), Proc. Int. Symp. Superalloys 2020, Springer US, Seven Springs, PA, USA, 2020: pp. 591–602.

[46] D. Texier, A. Casanova-Gómez, S. Pierret, J.M. Franchet, T.M. Pollock, P. Villechaise, J. Cormier, Microstructural Features Controlling the Variability in Low-Cycle Fatigue Properties of Alloy Inconel 718DA at Intermediate Temperature, Metall. Mater. Trans. A Phys. Metall. Mater. Sci. 47 (2016) 1096–1109.

[47] D. Texier, J. Cormier, P. Villechaise, J.C. Stinville, C.J. Torbet, S. Pierret, T.M. Pollock, Crack initiation sensitivity of wrought direct aged alloy 718 in the very high cycle fatigue regime: the role of non-metallic inclusions, Mater. Sci. Eng. A. 678 (2016) 122–136.

[48] A. Szczotok, K. Rodak, Microstructural studies of carbides in MAR-M247 nickel-based superalloy, IOP Conf. Ser. Mater. Sci. Eng. 35 (2012) 012006.

[49] L. Mataveli Suave, A. Serrano Muñoz, A. Gaubert, G. Benoit, L. Marcin, P. Kontis, P. Villechaise, J. Cormier, Thin-Wall Debit in Creep of DS200 + Hf Alloy, Metall. Mater. Trans. A. 49 (2018) 4021–4028.

[50] L. Mataveli Suave, High temperature durability of DS200+Hf alloy, PhD Thesis - Ecole Nationale Superieure de Mecanique et d'Aerotechnique (ISAE-ENSMA), France, 2017. https://www.theses.fr/2017ESMA0032.

[51] P. Berthod, Kinetics of High Temperature Oxidation and Chromia Volatilization for a Binary Ni–Cr Alloy, Oxid. Met. 64 (2005) 235–252.

[52] Y. Shida, G.C. Wood, F.H. Stott, D.P. Whittle, B.D. Bastow, Intergranular oxidation and internal void formation in Ni-40% Cr alloys, Corros. Sci. 21 (1981) 581–597.

[53] A.H. Rosenstein, J.K. Tien, W.D. Nix, Void Formation in Inconel MA-754 By High Temperature Oxidation., Metall. Trans. A, Phys. Metall. Mater. Sci. 17 A (1986) 151–162.

[54] J.H. Weber, P.S. Gilman, Environmentally induced porosity in NiCr and NiCr oxide dispersion strengthened alloys, Scr. Metall. 18 (1984) 479–482.

[55] H.E. Evans, Cavity formation and metallurgical changes induced by growth of oxide scale, Mater. Sci. Technol. (United Kingdom). 4 (1988) 1089–1098.

[56] E.O. Kirkendall, Diffusion of Zinc in Alpha Brass, Trans. Metall. Soc. AIME. 147 (1942) 104.

[57] C. Desgranges, F. Lequien, E. Aublant, M. Nastar, D. Monceau, Depletion and voids formation in the substrate during high temperature oxidation of Ni-Cr alloys, Oxid. Met. 79 (2013) 93–105.

[58] J. Ma, W. Jiang, J. Wang, Y. Zhang, Z. Zhang, Initial oxidation behavior of a single crystal superalloy during stress at 1150 °C, Sci. Rep. 10 (2020) 1–9.

[59] A.B. Parsa, M. Ramsperger, A. Kostka, C. Somsen, C. Körner, G. Eggeler, Transmission electron microscopy of a CMSX-4 Ni-base superalloy produced by selective electron beam melting, Metals. 6 (2016) 258.

[60] C. Juillet, A. Oudriss, J. Balmain, X. Feaugas, F. Pedraza, Characterization and oxidation resistance of additive manufactured and forged IN718 Ni-based superalloys, Corros. Sci. 142 (2018) 266–276.

[61] F. Pedraza, R. Troncy, A. Pasquet, J. Delautre, S. Hamadi, Critical Hafnium Content for Extended Lifetime of AM1 Single Crystal Superalloy, in: S. Tin, M.C. Hardy, J. Clews, J. Cormier, Q. Feng, J. Marcin, C. O'brien, A. Suzuki (Eds.), Proc. Int. Symp. Superalloys 2020, Springer US, Seven Springs, PA, USA, 2020: pp. 781–788.

[62] A. Hazotte, J. Lacaze, Chemically oriented γ′ plate development in a nickel base superalloy, Scr. Metall. 23 (1989) 1877–1882.

[63] L.M. Bortoluci Ormastroni, Ni-based single-crystal superalloy fatigue crack initiation shift from internal sites to the surface at high temperatures, PhD Thesis - École Nationale Supérieure de Mécanique et

d'Aérotechnique (ENSMA), 2022.

[64] H. Mayer, Fatigue crack growth and threshold measurements at very high frequencies, Int. Mater. Rev. 44 (1999) 1–34.

[65] W. Yang, S. Hu, M. Huo, D. Sun, J. Zhang, L. Liu, Orientation controlling of Ni-based single-crystal superalloy by a novel method: Grain selection assisted by un-melted reused seed, J. Mater. Res. Technol. 8 (2019) 1347–1352.

[66] K. Kawagishi, A.C. Yeh, T. Yokokawa, T. Kobayashi, Y. Koizumi, H. Harada, Development of an Oxidation-Resistant High-Strength Sixth-Generation Single-Crystal Superalloy TMS-238, in: E.S. Huron, R.C. Reed, M.C. Hardy, M.J. Mills, R.E. Montero, P.D. Portella, J. Telesman (Eds.), Int. Symp. Superalloys, TMS (The Minerals, Metals & Materials Society), Seven Springs, 2012: pp. 189–195.

[67] P. Caron, High gamma prime solvus new generation Nickel-based superalloys for single crystal turbine blade applications, in: T.M. Pollock, R.D. Kissinger, R.R. Bowman, K.A. Green, M. McLean, S. Olson, J.J. Schirra (Eds.), Proc. Int. Symp. Superalloys 2000, Springer US, Seven Springs, PA, USA, 2000: pp. 737–746.

[68] J. Rame, S. Utada, L.M. Bortoluci Ormastroni, L. Mataveli Suave, L. Despres, P. Kontis, J. Cormier, Platinum containing new generation nickel-based superalloys for single crystalline applications, in: S. Tin, M. Hardy, J. Clews, J. Cormier, Q. Feng, J. Marcin, C. O'brien, A. Suzuki (Eds.), Proc. Int. Symp. Superalloys 2020, Springer US, Seven Springs, PA, USA, 2020: pp. 71–81.